Received: 8 July 2024 | Revised: 22 November 2024 | Accepted: 14 December 2024

DOI: 10.1002/suco.202400886

ARTICLE

Machine learning for the prediction of the axial load-carrying capacity of FRP reinforced hollow concrete column

Jie Zhang[1] | **Walaa J. K. Almoghayer**[2] | **Haytham F. Isleem**[3,4] | **Bichitra Singh Negi**[5] | **Haitham A. Mahmoud**[6] | **Mohamed Kamel Elshaarawy**[7]

[1]School of Mechanical and Electrical Engineering, Xinxiang University, Xinxiang, China

[2]School of Business, Nanjing University of Information Science & Technology, Nanjing, China

[3]Department of Computer Science, University of York, York, UK

[4]Jadara University Research Center, Jadara University, Irbid, Jordan

[5]Department of Civil Engineering, Dev Bhoomi Uttarakhand University, Dehradun, India

[6]Department of Industrial Engineering, College of Engineering, King Saud University, Riyadh

[7]Civil Engineering Department, Faculty of Engineering, Horus University-Egypt, New Damietta, Egypt

Correspondence

Haytham F. Isleem, Department of Computer Science, University of York, York YO10 5DD, UK.
Email: mps565@york.ac.uk

Walaa J. K. Almoghayer, School of business, Nanjing University of Information Science & Technology, Nanjing, China.
Email: 202452250110@nuist.edu.cn

Funding information

King Saud University, Riyadh, Saudi Arabia, Grant/Award Number: RSPD2025R1006

Abstract

Fiber reinforced polymer (FRP) has emerged as a significant advancement in construction, with design provisions outlined by codes such as GB/T 30022-2013, CSA S806-12 (R2017), and ACI 440:2015. While the use of FRP bars as alternatives to conventional reinforcement in columns has been extensively studied, their application in hollow concrete columns (HCCs) remains underexplored. This study investigates the behavior of FRP-reinforced HCCs using advanced machine learning (ML) models, focusing on the prediction of two critical outputs: first peak load (Y1) and failure load (Y2), based on eight input parameters. Models evaluated include extreme gradient boosting (XGB), light gradient boosting (LGB), and categorical gradient boosting (CGB). A rigorous comparative analysis demonstrated that all models achieved high predictive accuracy, with deviations within ±10% of actual results, validating their reliability. Among the models, CGB exhibited superior generalization and robustness, emerging as the most reliable predictor for FRP-reinforced HCC behavior. To enhance practicality, a user-friendly graphical user interface was developed to allow engineers to input design parameters and instantly obtain predictions for Y1 and Y2. This study not only advances understanding of FRP-reinforced HCCs but also bridges the gap between computational predictions and real-world applications, contributing a robust predictive tool to structural engineering design.

KEYWORDS

prediction, failure load, fiber-reinforced polymer (FRP), hollow concrete column (HCC), machine learning (ML), SHapley additive exPlanations (SHAP)

1 | INTRODUCTION

Reinforced concrete (RC) is one of the promising materials which has several uses in the field of construction. In order to attain economic design and high strength-to-weight ratio, several researchers,[1,2] investigate the hollow RC structures, in which the investigation of hollow RC columns is most common. However due to changes in the environmental conditions, it get deteriorates due to corrosion, and with the passing of time results in the reduction of durability and hence, undergoes the retrofitting and rehabilitation of structures. To overcome these problems, fiber reinforced polymer (FRP) reinforced hollow RC structures are one of the promising solutions because of their high strength-to-weight ratio, corrosion resistance, and economical construction. In the construction of important structures like bridges, hollow RC columns can act as an alternative to solid concrete piers because it reduce the contribution of the mass of the column to the seismic response and reduce the load-carrying demand on the foundations.[3,4]

However, because of their anisotropic and nonhomogenous nature, FRP bars are still thought to be difficult to utilize in compression members. A few researchers,[5,6] have recently looked into the application of corrosion-free FRP reinforcement in hollow-core concrete columns. According to these investigations, FRP reinforcement outperformed steel reinforcement in hollow-core circular concrete columns because longitudinal FRP bars' greater axial strain capacity allowed them to support a greater axial load following the concrete cover's spalling.[5,6] Additionally, the concrete core was more successfully contained by the FRP-reinforced hoop bars than by the steel stirrups due to the higher tensile strength of FRP-reinforced hoop bars. Some of the researchers[7–10] investigated that the inclusion of FRP bars not only imparts the corrosion resistance but also enhances tensile strength up to 25%, because of its higher tensile yield strain than the traditional reinforcement bars. The same has been also verified by the ACI 440.[11]

Over the last few decades, different investigations[12–14] have been involved in conducting the test by incorporating FRP bars as a replacement of traditional reinforcement in the solid as well as HCCs. Almost all of them found that there is considerable increase in axial strength. Additionally, it has been shown that FRP columns exhibit significant strain hardening, ductility, and energy absorption capacity, even under high strain rates and large deformations Some of them used as lateral confinement and obtain the enhanced strength and ductility of the columns.[15] Researchers examined how FRP-reinforced HCCs responded experimentally to axial loading and contrasted their findings with those of conventional hollow RC columns. They discovered that the size and diameter of GFRP bars, the quantity of lateral reinforcement, the inner diameter to outer diameter ratio (*i*/*o*) of the columns, and the ratio of the actual load to the axial load-carrying capacity are the main factors influencing the structural axial response of hollow RC columns.[5,10]

Valuable research has been done over the past 20 years on the applications of fiber-reinforced polymers (FRPs) as strengthening and retrofitting materials for structures.[16–19] Additionally, FRP bars have been used as flexural and shear reinforcement for concrete structures.[12,20,21] Consequently, several design codes[11,22,23] have been created for the design of FRP-reinforced structures. Eventually, the usage of FRP bars and ties in compression members became the focus of various researchers. According to studies by Zhang et al.,[24] Liao et al.,[25] and Zeng et al.,[26] steel ties offer continuous confining pressure after the ties yield, while FRP ties exhibit a linear-elastic behavior up to failure, which improves their confining performance. Apart from the low compression resistance offered by the bars due to reduced elastic modulus under compression compared to steel, which is equally good in compression and tension,[25–28] the usage of longitudinal bars in compression members was also shown to be suitable.

In response to issues with solid sections and steel-reinforced HCCs, AlAjarmeh et al.[5] first presented circular HCC reinforced with FRP bars. On the other hand, a thorough understanding of the axial behavior of FRP-reinforced HCC is required for their practical application, as is the measurement of their mechanical attributes including strength, stiffness, and ductility. Nonetheless, it is preferable to switch to non-destructive testing when approaching sustainability as opposed to destructive experimental activity. Utilizing the most recent methods and tools is also essential to comprehending the behavior of HCC reinforced with fiber-reinforced polymer. As a result, over the past few years, a few researchers[10,26,29–31] have used machine learning (ML) and finite element modeling (FEM) techniques to study the behavior of reinforced with fiber-reinforced polymer (FRP).

Using ML to forecast models can cut down on the number of trials needed while managing the risks and expenses associated with these kinds of investigations. Numerous fields have successfully used ML to solve engineering difficulties[13,21,24,29,32–34] established a model that determined the priority among input parameters and proposed a new high-precision formula in order to conduct a sensitivity analysis on the performance of GFRP using the artificial neural network (ANN) method. Fei et al.[35] proposed an optimization model to estimate the bond strength of the GFRP columns by combining the global search capability of the genetic algorithm with the nonlinear mapping relationship of ANN. In order to test the theory that ML techniques offer a more understandable visual representation of failure modes in composite columns, Aravind et al.[36] subjected the beams to a four-point bending test, after which they processed the images and identified the fault modes using six distinct machine-learning techniques. A high-precision XGBoost model was developed to examine column performance after Bakouregui et al.[37] found that the XGBoost model outperforms other numerical models in estimating the bearing capacity of FRP-RC columns. Basaran et al.[38] looked into the bond strength and development length of FRP columns using a variety of machine-learning techniques, such as ANN, MLP, and SVMR.

However, it is quite limited and requires more exploration using cutting-edge approaches such as advanced ML models. This paper fills this research gap by doing a thorough numerical evaluation using the ML to better understand the performance of FRP-reinforced HCCs. The purpose of this study was to use ML techniques to examine parameters and the failure load of FRP-reinforced HCCs without the need for cumbersome, time-consuming, and destructive experimental tests. As a result, this paper is designed to provide a clear and thorough examination of FRP reinforcement in hollow concrete columns (HCC). Section 1: "Introduction," it gives an overview of FRP utilization in structural engineering and highlights the research aims. Section 2: "Research significance," it addresses the necessity of studying FRP-reinforced HCC, particularly in light of the scarcity of prior studies. Section 3: "Methodology," it explains the methodology used to simulate HCC behavior, including data gathering and ML approaches, as well as the parameters employed in prediction analysis. Section 4: "Results and discussion," shows findings from several models, including XGB, LGB, and CGB assesses model performance in forecasting load capacities. Finally, Section 5: "Conclusions," it summarizes the study's main outcomes, emphasizing the potential of the robust predictive model, and suggests future research directions for FRP applications in structural engineering.

2 | RESEARCH SIGNIFICANCE

The few investigations have been done for design of FRP-reinforced HCC. Additionally, the design codes have incorporated the provisions for FRP RC column but none of them includes the provisions of FRP-reinforced HCC. Therefore, in order to obtain optimized design and recommendations of proper guidelines, a lot of investigation is needed in this field, and keeping in view of present scenario, more advanced techniques are necessary to achieve accurate, optimized, risk-free results with sustainable construction. Hence, the following are the authors' specific contributions: (1) Advanced ML models are introduced and their effectiveness in predicting the target outputs is thoroughly evaluated; (2) Predictive accuracy is significantly enhanced through hyperparameter tuning using Bayesian optimization (BO); (3) A comprehensive performance evaluation is conducted, incorporating both visual methods (scatter plots, regression error characteristics (REC), violin plots, and Taylor diagrams) and quantitative analyses (uncertainty evaluation and regression metrics) to assess the predictive capabilities of the models; (4) SHapley Additive Explanations (SHAP) and partial dependence plot (PDP) analyses are utilized to determine the key parameters that most significantly influence discharge prediction; (5) To bridge the gap between computational predictions and practical real-world applications, a user-friendly graphical user interface (GUI) is developed, enabling engineers to efficiently predict the outputs with ease and practicality.

3 | METHODOLOGY

Within the vast domain of artificial intelligence (AI), ML and deep learning (DL) are established as progressive subsets that delve deeper into the capabilities of automated data processing and pattern recognition.[39] ML represents a significant advancement in AI, where algorithms learn from data and make predictions.[40] ML models identify trends and patterns through iterative learning from input data, improving with experience akin to human knowledge. These models excel at handling structured datasets and performing various tasks, from classification to regression, without specific programming for each task's nuances. In this study, three advanced ML models: extreme gradient boosting (XGB), light gradient boosting (LGB), and categorical gradient boosting (CGB) was conducted using the Python programming environment within the Anaconda software.[41–43] The ensemble techniques boost the performance metrics of predictive models, notably diminishing error rates and increasing higher correlations between predicted and actual values. The improvement in the model's performance can be credited to the ensemble's ability to mitigate issues like underfitting, overfitting, or the lack of unity between the model and the dataset.

3.1 | Dataset description

The dataset contains 144 samples and documented in the Appendix A (Table A1). It is designed to support the development of the adopted models to predict the first peak load ($P_{n,1}$, kN) and failure load ($P_{n,2}$, kN) of FRP-RC HCCs using a final dataset of 144 data points with 8 input features and 2 output features. The compressive strength of the standard cylinder (f_o, MPa), the diameter of the internal hole (D_o, mm), the outer diameter of the HCC (D, mm), the column's height (H, mm), the center to center spacing of hoop reinforcing bars (S', mm), area of FRP reinforcing hoop bar (A_b, mm^2), the tensile strength of FRP hoop bar (f_h, MPa), the ratio of longitudinal FRP reinforcing bars multiplied by its tensile strength ($\rho_v f_v$, MPa). These variables were designated as X1, X2, X3, X4, X5, X6, X7, and X8, respectively. $P_{n,1}$ and $P_{n,2}$ were considered the outputs and denoted Y1 and Y2, respectively.

3.1.1 | Statistical summary

To provide a foundational understanding of the dataset utilized in this study, Table 1 presents the descriptive statistics for the input variables (X1 to X8) and the output variables (Y1 and Y2), providing a summary of their distributions in terms of minimum (Min), maximum (Max), mean, median, and standard deviation (SD) values. These statistics offer insight into the variability and central tendencies of the dataset, which are crucial for understanding the underlying data characteristics and their potential influence on predictive modeling.[44]

Considering the input variables, X1 (f_o, MPa) represents a parameter with a minimum value of 21.20 and a maximum value of 70.20, with a mean of 31.03 and a SD of 10.43. These values suggest that X1 exhibits moderate variability, as evidenced by its SD relative to its range. X2 (D_o, mm) has a wide range from 0.00 to 120.00, a mean of 54.21, and a SD of 40.39, indicating significant variability and potential skewness, as its median (60.00) is slightly higher than the mean. Similarly, X3 (D, mm) ranges from 205.00 to 305.00 with a mean of 252.33 and a SD of 25.58, showing a relatively narrow distribution around the mean. X4 (H, mm) spans a very broad range from 800.00 to 3000.00, with a mean of 1457.64 and a high SD of 619.65, reflecting substantial variability and dispersion around its median (1150.00). Other input variables, such as X5 (S', mm), range from 0.00 to 200.00, with a mean of 98.89 and a SD of 43.33, showing moderate variability. X6 (A_b, mm^2), with a narrower range of 50.29 to 81.50, has a mean of 70.87 and a small SD of 5.91, indicating that its values are tightly clustered around the mean. X7 (f_h, MPa) demonstrates a broader range, from 975.00 to 1562.00, with a mean of 1309.73 and a SD of 110.72, suggesting moderate variability. Finally, X8 (ρ_v f_v, MPa) ranges from 6.04 to 77.97, with a mean of 35.78 and a SD of 14.68, showing moderate spread in its distribution.

Considering the output variables, Y1 ($P_{n,1}$, kN) and Y2 ($P_{n,2}$, kN), the ranges are from 842.01 to 4716.00 and 707.25 to 4222.37, respectively. Y1 has a mean of 1544.78 and a SD of 884.82, while Y2 has a mean of 1548.23 and a SD of 802.17. These high standard deviations relative to their means indicate considerable variability in the output variables, which is expected given the range of the inputs and their potential influence on the outputs. Overall, the descriptive statistics indicate a diverse dataset with varying degrees of variability among the input and output variables. Inputs such as X4, X2, and X7 show significant dispersion, which could have a substantial impact on the outputs. Meanwhile, inputs like X6 display relatively low variability, suggesting a more stable influence.

3.1.2 | Hexbin graphs

Figure 1 presents hexbin plots to visualize the relationships between the eight input variables (X1 to X8) and the two output variables (Y1 and Y2). Hexbin plots are particularly useful for examining the density and distribution of data points in a two-dimensional space, providing insight into patterns and correlations while highlighting areas with higher concentrations of data. In the plots for Y1 (top figure), distinct patterns are observed across the input variables. For X1, the distribution of data

TABLE 1 Descriptive statistics of the input and output variables.

Input	Unit	Symbol	Min	Max	Mean	Median	SD
f_o	MPa	X1	21.20	70.20	31.03	31.80	10.43
D_o	mm	X2	0.00	120.00	54.21	60.00	40.39
D	mm	X3	205.00	305.00	252.33	250.00	25.58
H	mm	X4	800.00	3000.00	1457.64	1150.00	619.65
S'	mm	X5	0.00	200.00	98.89	100.00	43.33
A_b	mm^2	X6	50.29	81.50	70.87	70.80	5.91
f_h	MPa	X7	975.00	1562.00	1309.73	1315.00	110.72
$\rho_v f_v$	MPa	X8	6.04	77.97	35.78	34.31	14.68
$P_{n,1}$	kN	Y1	842.01	4716.00	1544.78	1204.06	884.82
$P_{n,2}$	kN	Y2	707.25	4222.37	1548.23	1299.50	802.17

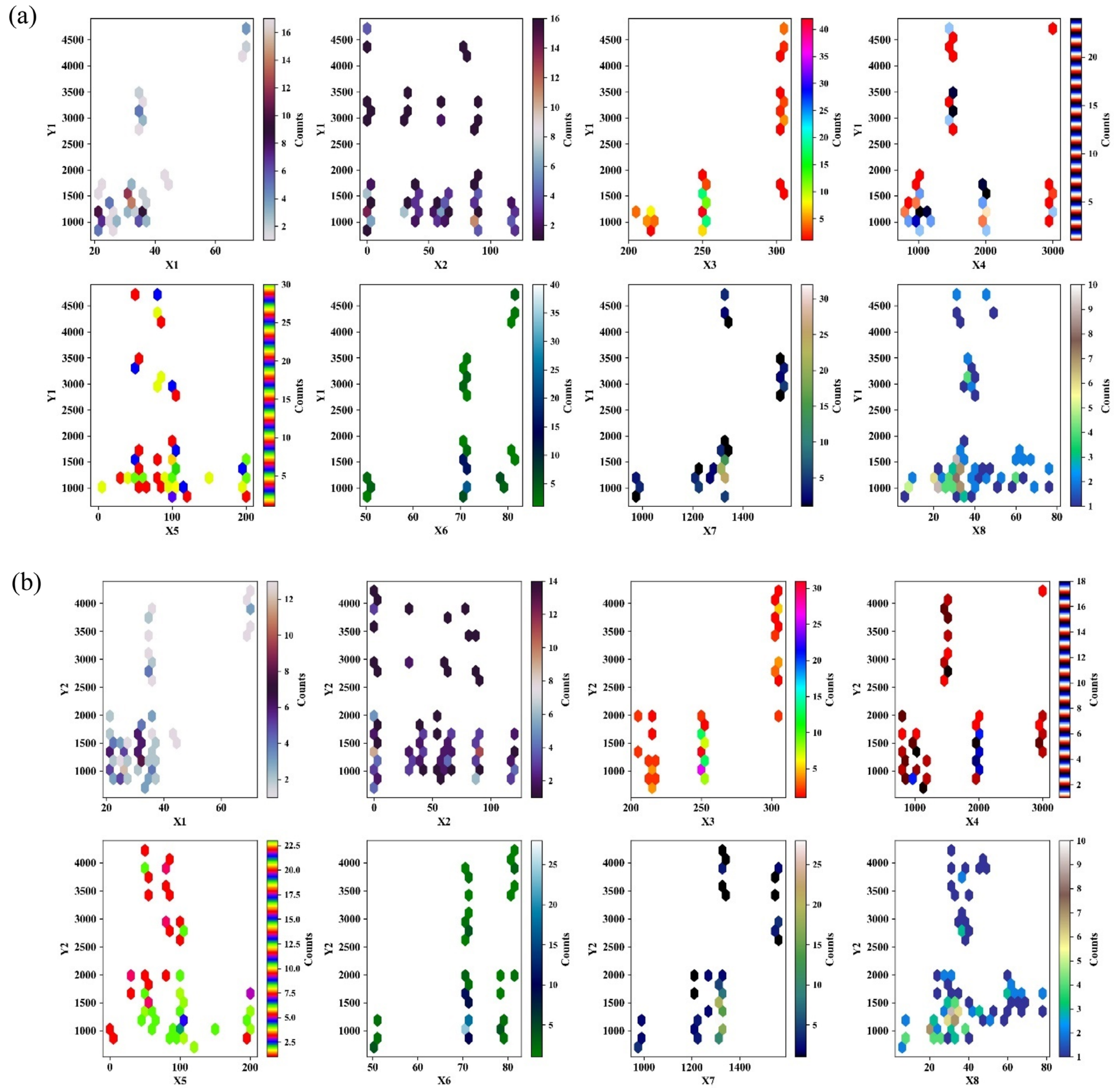

FIGURE 1 Hexbin graphs of input variables versus (a) Y1 and (b) Y2.

points shows a noticeable trend where higher values of X1 correspond to increased values of Y1, indicating a positive correlation. Similar behavior is seen for X3 and X7, where the higher values of these inputs are associated with larger Y1 values, suggesting these variables are significant predictors for Y1. For X2, X4, and X5, the distributions are more dispersed, with no distinct trend connecting their values to Y1. This indicates a weaker or less direct influence of these variables on Y1. X6 and X8 show moderate clustering, where specific ranges of these inputs seem to correspond to certain Y1 values, suggesting a more conditional or nonlinear relationship. In the plots for Y2 (bottom figure), the trends are somewhat consistent with those observed for Y1, with X1, X3, and X7 again showing strong associations with Y2. Higher values of these inputs generally align with higher Y2 values, confirming their predictive significance. However, the influence of X2, X4, and X5 appears less prominent, with scattered data points and no clear patterns of correlation. For X6 and X8, clustering patterns suggest that certain input ranges may impact Y2, though the relationship is less straightforward than for X1, X3, and X7.

The color gradients in the hexbin plots represent the density of data points within each hexagonal bin. Darker or more intense colors signify higher concentrations of data points, highlighting regions with significant data clustering. For both Y1 and Y2, the clustering patterns reflect the dataset's structure, revealing which input ranges are more frequent and how they correspond to the outputs. The observed trends underscore the importance of variables such as X1, X3, and X7 while indicating weaker or more complex relationships for other inputs. These findings can inform feature selection and modeling strategies to optimize predictions for Y1 and Y2.

3.1.3 | Correlation analysis

The heatmap in Figure 2 not only highlights the correlation between the input variables (X1 to X8) and the output variables (Y1 and Y2) but also reveals the interrelationships among the input variables themselves. As shown in the heatmap, the relationships between the inputs and outputs, X1, X3, and X7 stand out as the most influential predictors for both Y1 and Y2. For Y1, X1 exhibits the highest positive correlation (0.81), followed closely by X3 (0.79) and X7 (0.48). This suggests that increases in these variables lead to significant increases in Y1. A similar pattern is observed for Y2, where X3 has the strongest correlation (0.77), followed by X1 (0.70) and X7 (0.55). These results indicate that these three variables serve as critical drivers for both output variables, making them prime candidates for further analysis and feature importance evaluation. X2 shows a weak negative correlation with both Y1 (−0.25) and Y2 (−0.26), indicating that it has an inverse and less significant effect on the outputs. Similarly, variables such as X4, X5, and X8 demonstrate much weaker correlations with both outputs, ranging between −0.2 and 0.3. These results suggest that these inputs have either negligible or highly indirect influences on the prediction of Y1 and Y2.

Examining the interrelationships among the inputs themselves reveals a complex structure of dependencies.[45] For instance, X3 and X7 have a strong positive correlation (0.76), indicating that these variables share similar trends or information. This strong interdependence could potentially lead to multicollinearity issues when included in predictive models. X6 also shows moderate positive correlations with X3 (0.38) and X7 (0.53), suggesting it shares some predictive patterns with these variables, albeit to a lesser degree. In contrast, X2 demonstrates weak or negative correlations with most other input variables, particularly with X1 (−0.22) and X4 (−0.11). This indicates that X2's behavior is distinct and relatively independent from other inputs. The observed interrelationships among inputs can influence the modeling process. Variables with high correlations, such as X3 and X7, may introduce redundancy in the model, and techniques like feature selection or dimensionality reduction might be necessary to address this issue. Conversely,

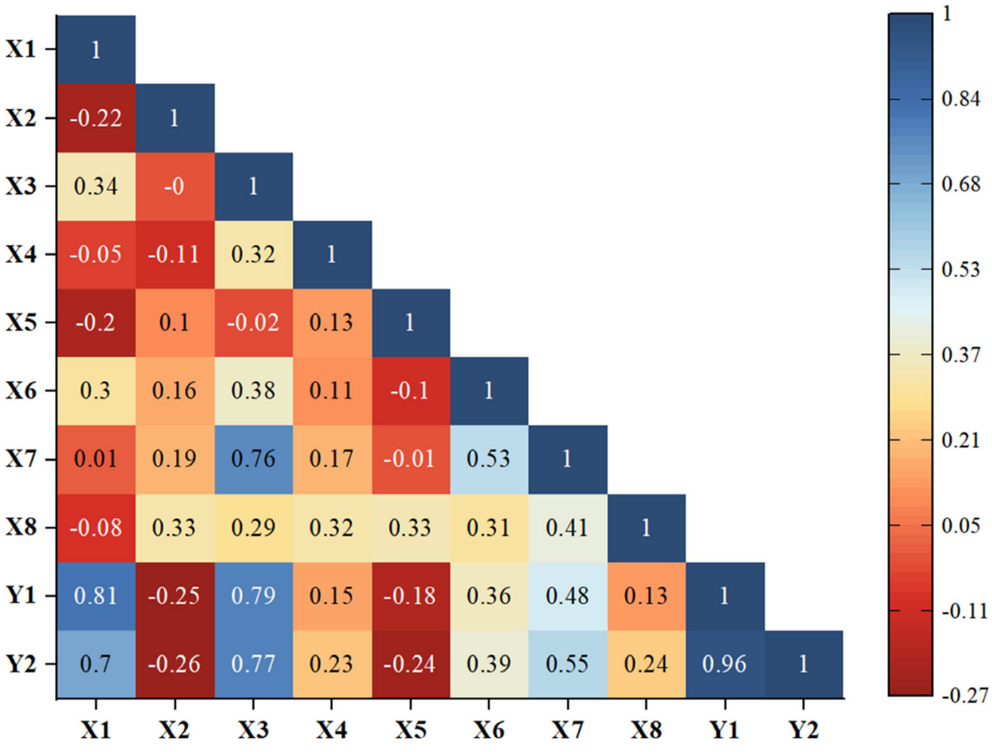

FIGURE 2 Heatmap indicating correlation values of inputs versus (a) Y1 and (b) Y2.

inputs like X2, which are less correlated with others, may offer unique and complementary information to the model, despite their weaker correlation with the outputs. Overall, the heatmap highlights the intricate web of relationships between the inputs and outputs. It emphasizes the importance of variables such as X1, X3, and X7 in driving the outputs while suggesting that variables like X2, X4, X5, and X8 may have more limited roles. Additionally, the interdependencies among inputs underscore the need to carefully evaluate feature contributions and manage multicollinearity to ensure robust and interpretable predictive models.

3.2 | Description of ML models

XGBoost is a highly effective and versatile ML library that excels in handling large datasets and complex predictive modeling tasks.[46] Its ability to handle missing values, regularization techniques, and parallel processing capabilities make it a reliable choice for various applications. With its high accuracy, speed, and scalability, XGBoost is a popular choice for many industries, including finance, computer vision, and natural language processing.[47] Overall, XGBoost is a powerful tool for data scientists and ML engineers, offering a robust and efficient way to build predictive models that can drive business decisions and improve outcomes. LightGBM is a fast and efficient gradient-boosting framework well-suited for large-scale ML tasks.[48] It is designed to be quicker and more scalable than other popular gradient-boosting libraries, such as XGBoost while maintaining similar performance. LightGBM is known for its ability to handle large datasets and complex models efficiently, making it a popular choice for many applications, including classification, regression, and ranking tasks.[49] CatBoost is an advanced, open-source gradient-boosting library optimized for categorical data, integrating decision trees with gradient-boosting methods. It directly incorporates categorical features, reducing the need for extensive pre-processing and enhancing model accuracy. Renowned for its high performance in various prediction tasks, CatBoost effectively minimizes overfitting and improves model generalization, making it suitable for regression applications.[50]

3.3 | Hyperparameters tuning

Hyperparameter tuning using BO is a sophisticated method for optimizing ML models.[51,52] Unlike brute force or grid search methods, BO intelligently explores the hyperparameter space by leveraging probabilistic models. It begins with an initial set of hyperparameters and evaluates their performance using a chosen metric.[53] Based on these results, BO updates its probabilistic model to predict which hyperparameters will yield better performance. It then selects new hyperparameters to evaluate, balancing exploring new regions with exploiting known good areas. This iterative process continues until satisfactory hyperparameters are found. By dynamically adapting to the model's performance, BO offers a more efficient and effective approach to hyperparameter tuning, saving time and resources while maximizing model performance.[54]

3.4 | Performance metrics

Assessing the effectiveness of each model is essential to ensure the practicality and scientific reliability of the outcomes.[55–57] While training datasets help construct models, they only reveal how well they fit the given data. Therefore, testing datasets are crucial for validating the models. Evaluation and comparison of models typically involve two main methods: visual and quantitative assessments. Visual methods include scatter plots, violin boxplots, and Taylor diagrams, which offer quick insights into the accuracy prediction of various statistical measures such as maximum, minimum, median, and quartiles.[58,59] Unlike quantitative metrics, which may not capture these aspects, visual methods provide rapid, engaging, and informative comparisons. As a result, three quantitative metrics were utilized: determination coefficient (R^2), RMSE, and mean absolute error (MAE). The equations for these performance metrics and their ideal values are listed in Table 2.

Moreover, an uncertainty analysis is conducted as it is a crucial component of model evaluation, providing insight into the reliability and robustness of predictions by quantifying the confidence intervals around predicted values. It is particularly important in applications where accurate and consistent predictions are critical, as it helps identify the range of potential errors and ensures the

TABLE 2 Equations of performance metrics and their ideal values.

Metric	Equation	Ideal value
Determination coefficient (R^2)	$R^2 = \frac{\sum_{i=1}^{n}(y_i - y_{\text{mean}})^2 - \sum_{i=1}^{n}\left(y_i - \widehat{y_i}\right)^2}{\sum_{i=1}^{n}(y_i - y_{\text{mean}})^2}$	1
Root mean square error (RMSE)	$\text{RMSE} = \sqrt{\frac{\sum_{i=1}^{n}\left(y_i - \widehat{y_i}\right)^2}{n}}$	0
Mean absolute error (MAE)	$\text{MAE} = \frac{\sum_{i=1}^{n}\left\lvert y_i - \widehat{y_i}\right\rvert}{n}$	0

Note: Where n is the dataset number y_i and $\widehat{y_i}$ are actual and predicted ith values, respectively.

model's outputs are interpretable and dependable. One commonly used metric for expressing uncertainty is the 95% uncertainty interval (U_{95}), which captures the range within which 95% of the prediction errors are expected to fall. U_{95} is calculated using the RMSE and the SD of the prediction values, combining these metrics to reflect both the average error magnitude and the spread of the predictions.[60] During the training stage, U_{95} provides an indication of the model's ability to fit the data and minimize variability, while in the testing stage, it reflects the model's generalization capability to unseen data. A narrower U_{95} indicates higher model reliability and lower variability in predictions, while a broader U_{95} suggests greater uncertainty and less consistent performance. By evaluating U_{95} across both training and testing stages, researchers can assess not only the predictive accuracy of the model but also the confidence in its outputs, enabling informed decisions based on the model's predictions.

3.5 | Feature interpretation and importance analysis

SHAP values are derived from cooperative game theory and offer a unified approach to interpreting ML models.[13,41] The core concept behind SHAP is to fairly distribute the prediction among the input features by assigning an "importance value" to each feature, representing its contribution to the overall prediction. This is achieved by calculating the marginal contribution of each feature across different subsets of the input features, ensuring a consistent measure of feature importance. One of the key advantages of SHAP is its ability to provide local interpretability, meaning it can explain individual predictions rather than just general trends across the dataset. This allows practitioners to understand why the model made a specific prediction for a given instance, thereby enhancing transparency. Moreover, SHAP values are consistent and additive, making them a reliable tool for feature importance analysis in complex, non-linear models.

Partial dependence plots (PDPs), on the other hand, are graphical representations that help to visualize the relationship between one or more input features and the predicted outcome of a ML model.[61] By averaging out the effects of other features, PDPs depict how changes in a specific feature, or a pair of features influence the model's predictions. This enables researchers to interpret the global behavior of the model with respect to the selected features. PDPs are particularly useful for understanding the direction and magnitude of feature influence. For example, they can reveal whether an increase in a particular feature value leads to higher or lower predictions and whether this relationship is linear, monotonic, or more complex. However, PDPs assume feature independence, which can sometimes limit their effectiveness when features are strongly correlated. Despite this, PDPs remain a valuable tool for assessing feature importance and gaining insight into the model's predictive patterns.

4 | RESULTS AND DISCUSSION

4.1 | Optimal hyperparameters

Table 3 provides a detailed overview of the optimized hyperparameters for the adopted ML models to predict Y1 and Y2. The hyperparameters for each model were carefully tuned based on the BO method to achieve the best predictive performance for both outputs. For the XGBoost model, several key hyperparameters were optimized. The number of trees in the model (n_estimators) was set to 939 for predicting Y1 and 955 for predicting Y2. The maximum depth of each tree (max_depth) was set to 3 for both outputs. The step size for updating weights (learning_rate) was set at 0.171 for Y1 and increased to 0.266 for Y2. Additionally, the fraction of features to consider for each tree (colsample_bytree) was set to 0.945 for Y1 and slightly adjusted to 0.934 for Y2. The sample fraction for fitting each tree (subsample) was set to 0.915 for Y1 and 0.919 for Y2. The LightGBM model's hyperparameters also underwent optimization. The maximum number of leaves in one tree (num_leaves) was set to 100 for Y1 and significantly reduced to 10 for Y2. The learning rate for LGB was set to 0.2 for Y1 and increased to 0.262 for Y2, reflecting the adjustment needed to achieve better performance for the second output. The number of trees was set to 633 for Y1 and 1000 for Y2, showing a substantial increase for the latter. For the CatBoost model, the hyperparameters remained consistent for both outputs, reflecting the model's stability across different tasks. The depth of each tree was set to 3 for both Y1 and Y2. The learning rate was set to 0.254 for Y1 and slightly increased to 0.262 for Y2. Finally, the L2 regularization on leaf weights (l2_leaf_reg) was set to 1 for both outputs.

4.2 | Visual performance assessment

4.2.1 | REC curves

Figure 3 presents cumulative distribution plots for residual errors obtained from three ML models during both the training and testing stages for two output variables (Y1 and Y2). The cumulative distribution functions (CDFs) provide a detailed assessment of the models' error distributions and their predictive performance. In the training stage for Y1 (Figure 3a), the performance of

TABLE 3 Optimized hyperparameters for the adopted ML models in predicting the two outputs.

Model	Output 1 (Y1)	Output 2 (Y2)
XGB	n_estimators = 939 max_depth = 3 learning_rate = 0.171 colsample_bytree = 0.945 subsample = 0.915	n_estimators = 955 max_depth = 3 learning_rate = 0.266 colsample_bytree = 0.934 subsample = 0.919
LGB	num_leaves = 100 learning_rate = 0.2 n_estimators = 633	num_leaves = 10 learning_rate = 0.262 n_estimators = 1000
CGB	depth = 3 learning_rate = 0.254 l2_leaf_reg = 1	depth = 3 learning_rate = 0.262 l2_leaf_reg = 1

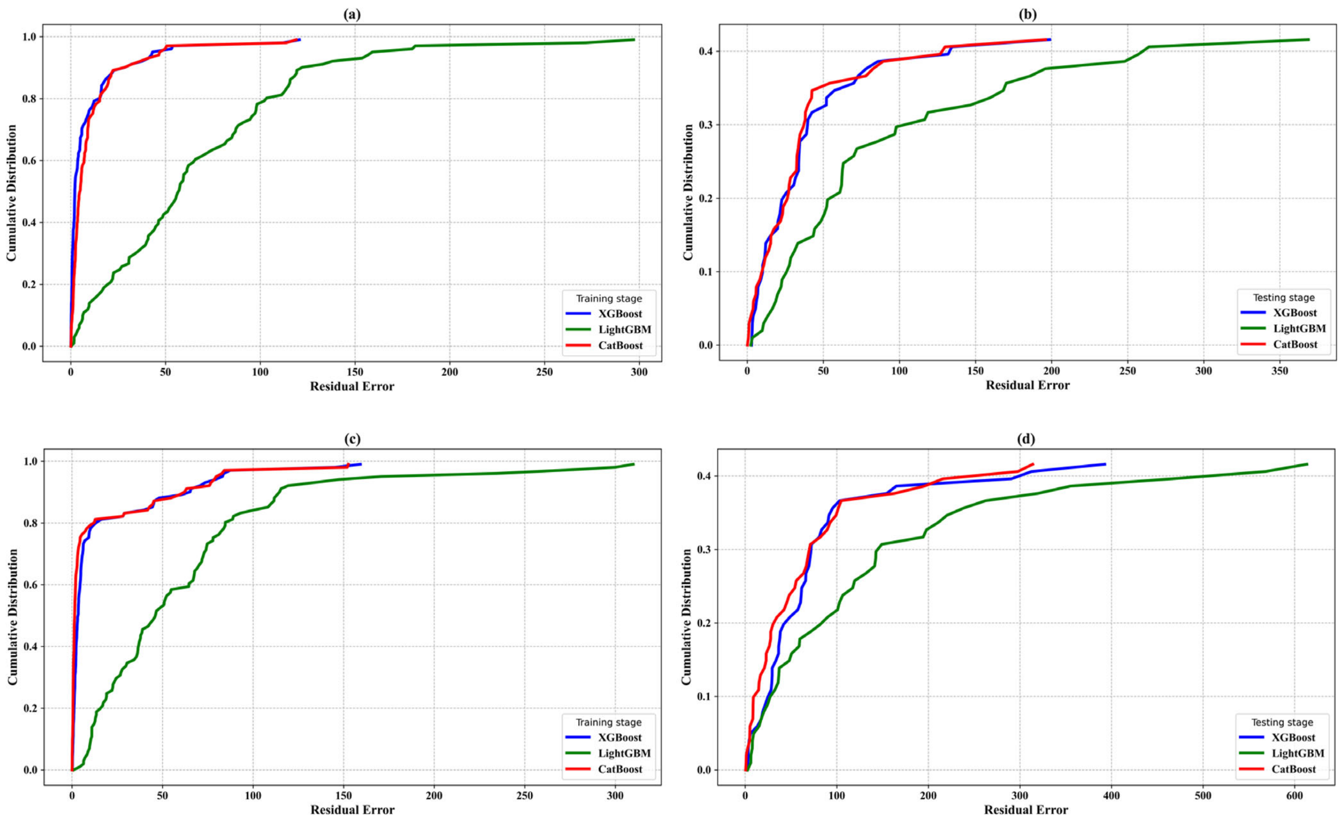

FIGURE 3 Regression error characteristics (REC) curves for Y1 in the (a) training and (b) testing stages; and for Y2 in the (c) training and (d) testing stages.

XGBoost and CatBoost appears nearly identical, as their CDF curves overlap significantly, reflecting similar error distributions. However, LightGBM displays larger residual errors for a substantial fraction of predictions, evidenced by the delayed rise in its CDF curve. The testing stage for Y1 (Figure 3b) reveals a similar trend, with XGBoost and CatBoost maintaining their advantage over LightGBM in terms of error distribution. However, all three models show slightly extended error distributions in the testing phase, as expected due to the challenges of generalizing to unseen data. Figure 3c and d correspond to the training and testing stages for Y2. As in the case of Y1, XGBoost, and CatBoost outperform LightGBM, with their CDF curves rising more sharply and reaching cumulative distributions near 1 at smaller residual error values. In the training stage (Figure 3c), CatBoost demonstrates slightly better error performance compared to XGBoost, as its curve reaches a higher cumulative distribution at lower residual errors. LightGBM again trails both models, with a flatter curve and residual errors spread over a wider range. In the testing stage for Y2 (Figure 3d), the trends remain consistent, with XGBoost and CatBoost retaining their advantage. However, the spread of residual errors increases for all models, as indicated by the broader distribution along the residual error axis. LightGBM shows the poorest performance in terms of error distribution, with its CDF curve rising more gradually and extending further along the error axis.

Overall, the plots highlight the superior predictive performance of XGBoost and CatBoost over LightGBM for both outputs, Y1 and Y2, during both training and testing stages. The results suggest that XGBoost and CatBoost consistently produce predictions with lower residual errors, making them more reliable for this dataset. These observations provide valuable insights into the error characteristics of the models and reinforce the importance of using robust evaluation metrics to assess predictive accuracy.

4.2.2 | Scatter plots

Figure 4 presents scatter plots comparing the actual versus predicted values for two output variables (Y1 and Y2) across three ML models during both training and testing phases. For Y1, Figure 4a–c correspond to XGBoost, LightGBM, and CatBoost, respectively. In Figure 4a, XGBoost achieves excellent performance in both training and testing stages, with an R^2 value of 1.00 for training and 0.97 for testing, indicating a nearly perfect fit during training and high generalization accuracy during testing. The RMSE and MAE values in the testing phase are relatively low (54.03 and 36.79 kN, respectively), further confirming the model's robustness. The predicted points closely align with the equality line (45° line), with minimal scatter beyond the ±10% deviation lines, demonstrating high prediction accuracy. In Figure 4b, LightGBM exhibits slightly lower performance than XGBoost. The R^2 value for testing is 0.93, indicating a reduced ability to capture the variance in the testing data. The RMSE and MAE values are higher at 119.81 and 86.39 kN, respectively, reflecting greater residual errors. The scatter points deviate more from the equality line compared to XGBoost, particularly for higher actual Y1 values, suggesting potential limitations in LightGBM predictive capability for this dataset. Figure 4c illustrates the performance of CatBoost, which closely rivals XGBoost. The R^2 value is 0.98 for testing, and the RMSE and MAE values (52.09 and 34.95 kN, respectively) are comparable to those of XGBoost. The predicted points are densely clustered along the equality line, with only minor deviations, indicating that CatBoost effectively predicts Y1 with high accuracy. The model shows strong generalization across the training and testing datasets.

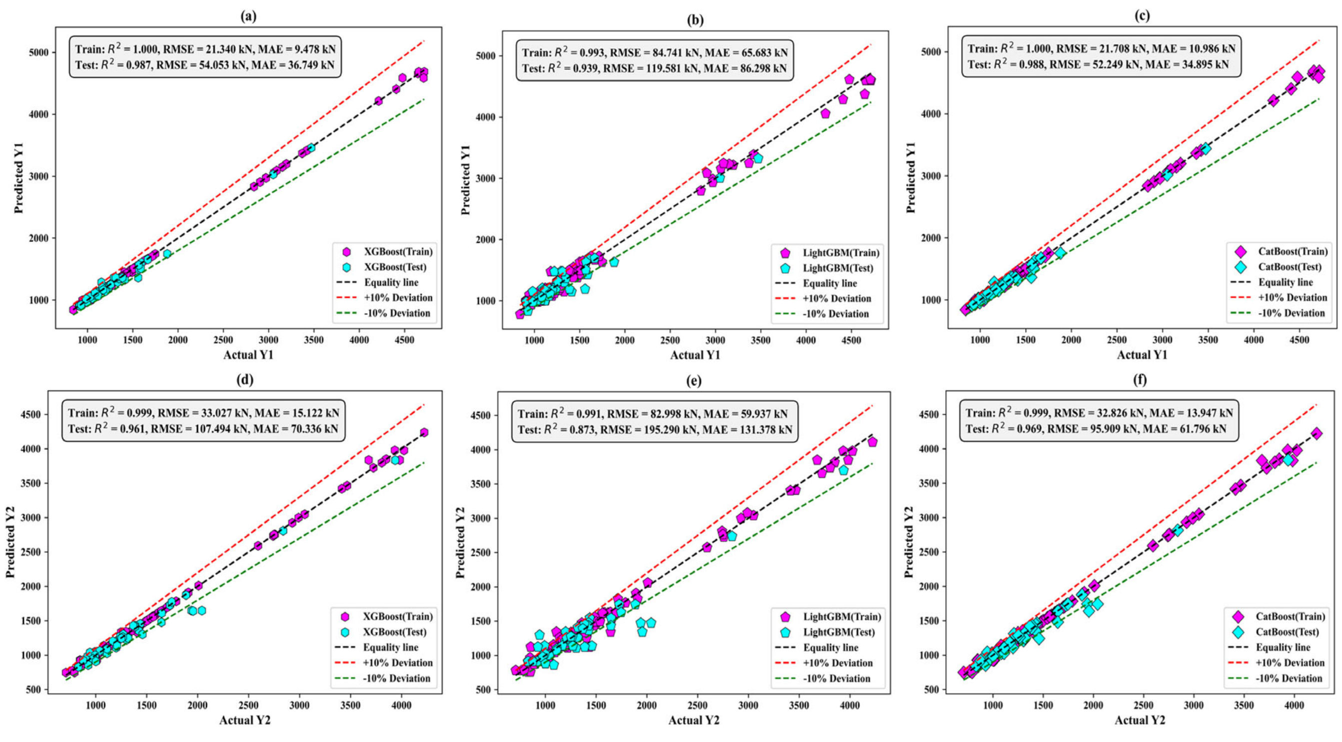

FIGURE 4 Performance scatter plots for Y1 based on (a) XGB, (b) LGB, and (c) CGB; for Y2 based on (d) XGB, (e) LGB, and (f) CGB.

For Y2, Figure 4d–f correspond to XGBoost, LightGBM, and CatBoost, respectively. In Figure 4d, XGBoost again demonstrates strong predictive performance, with an R^2 value of 0.94 for testing and relatively low RMSE (107.49 kN) and MAE (70.43 kN) values. The scatter points show good alignment with the equality line, though slight deviations are observed, particularly for higher Y2 values. These results indicate reliable predictive capabilities, albeit with slightly larger errors compared to Y1. In Figure 4e, LightGBM displays reduced accuracy for Y2 compared to XGBoost and CatBoost. The testing R^2 value is 0.87, with higher RMSE (193.20 kN) and MAE (131.81 kN) values, suggesting a larger degree of error in predictions. The scatter points exhibit noticeable dispersion around the equality line and frequently fall outside the ±10% deviation lines, indicating weaker performance in capturing Y2's variance. Figure 4f demonstrates that CatBoost maintains strong performance for Y2, similar to its results for Y1. The testing R^2 value is 0.90, with RMSE and MAE values (89.90 and 61.70 kN, respectively) lower than those of LightGBM and comparable to XGBoost. The scatter points closely follow the equality line, with minimal dispersion, reflecting CatBoost's reliability and accuracy for predicting Y2. Overall, the scatter plots reveal that XGBoost and CatBoost outperform LightGBM in terms of both predictive accuracy and error metrics for Y1 and Y2. The alignment of predicted values with the equality line, along with low RMSE and MAE values, underscores the effectiveness of XGBoost and CatBoost in modeling the dataset. LightGBM, while still effective, shows comparatively weaker performance, particularly for the testing data, with higher residual errors and greater deviations from the equality line.

4.2.3 | Violin boxplots

Figure 5 presents violin plots that visualize the distribution of predictions for the first peak load ($P_{n,1}$) and the failure load ($P_{n,2}$) using the three adopted models, that is, XGBoost (XGB), LightGBM (LGB), and CatBoost (CGB), alongside the actual test data (TS). The violin plots provide a detailed representation of the data distribution, combining kernel density estimation with boxplot elements to show the spread, central tendency, and variability of the predictions and actual values. In Figure 5a, which corresponds to $P_{n,1}$, the violin plots reveal that all three models successfully capture the general distribution of the actual test data. XGBoost and CatBoost exhibit narrower distributions, suggesting higher consistency and lower variability in their predictions. Their median predictions (XGBoost: 1180.54 kN, CatBoost: 1188.86 kN) closely align with the actual median (1173.78 kN). The interquartile ranges (IQRs), represented by the white boxplots within the violins, are also comparable to the actual data, indicating that these models can reliably predict values within the central range. LightGBM, on the other hand, shows a broader distribution, with its median (1173.93 kN) still close to the actual TS but with slightly more variation in predictions. The tails of the distributions suggest that LightGBM is more prone to occasional over- or under-predictions compared to XGBoost and CatBoost. In Figure 5b, representing $P_{n,2}$, a similar pattern is observed. XGBoost and CatBoost again demonstrate narrower distributions, with median values (XGBoost: 1257.91 kN, CatBoost: 1260.24 kN) that align closely with the actual median (1269.99 kN). Their IQRs are consistent with the actual test data, and their distributions are tightly centered around the median,

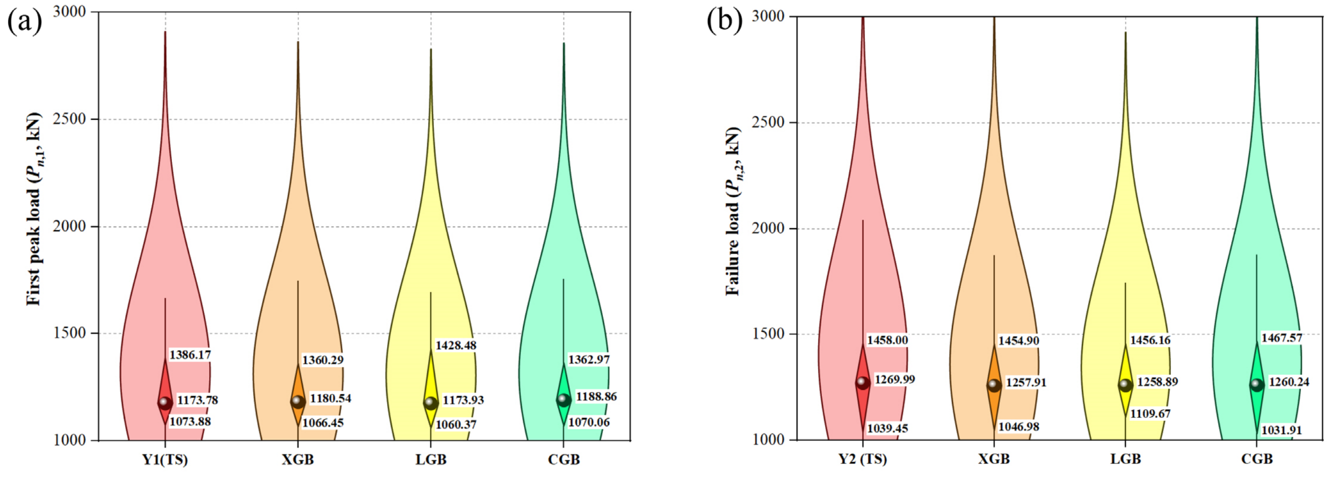

FIGURE 5 Violin boxplots during the testing phase for (a) Y1 and (b) Y2.

indicating reliable and accurate predictions. LightGBM, while capturing the general distribution, exhibits a wider spread (median: 1258.89 kN), with a larger proportion of its predictions falling in the tails of the distribution. This suggests that LightGBM, although effective, is less consistent in predicting extreme values compared to XGBoost and CatBoost. Overall, the violin plots highlight the alignment of the models' predictions with the actual data through the positioning of the median and the range of variability. Both XGBoost and CatBoost exhibit superior predictive performance, as evidenced by their tight distributions and close agreement with the actual test data. LightGBM, while capturing the central tendency, shows slightly higher variability and a broader range of predictions. These findings reinforce the robustness of XGBoost and CatBoost in capturing the behavior of both $P_{n,1}$ and $P_{n,2}$ with high precision and consistency during the testing phase.

4.2.4 | Taylor diagrams

Taylor diagrams are a specialized graphical representation that quantifies the similarity between actual and predicted values. These diagrams plot the correlation, the standard deviation, and the root mean square error of predictions on a single chart. This provides a comprehensive view of a model's accuracy, variability, and overall performance compared to the actual observations. Figure 6 shows the Taylor diagrams during the testing phase for Y1 and Y2. Figure 6a shows the Taylor diagram for Y1. The XGB model has a SDof 476.71 kN and a correlation coefficient of 0.994, indicating a strong linear relationship with the TS dataset and moderate prediction variability. The LGB model exhibits the lowest SDat 467.93 kN but has a lower correlation coefficient of 0.969, suggesting less accurate predictions despite minimal variability. The CGB model balances a low SD of 473.99 kN with the highest correlation coefficient of 0.995, making it the most accurate and reliable predictor for Y1. Therefore, CGB is the best model for predicting Y1, demonstrating the closest alignment with the TS dataset. Figure 6b shows the Taylor diagram for output Y2, evaluating the performance of the same three models against the TS dataset. The XGB model has a SD of 521.67 kN and a correlation coefficient of 0.984, indicating a strong linear relationship and relatively accurate predictions. The LGB model has the lowest SD at 487.21 kN, suggesting less variability. However, its correlation coefficient of 0.942 is significantly lower than that of XGB and CGB, indicating less accurate predictions. The CGB model, with a SD of 523.84 kN and a correlation coefficient of 0.987, shows the highest reliability and accuracy in predictions. In summary, while the CGB model remains the best predictor for output Y2 due to its highest correlation coefficient and balanced standard deviation, XGB also demonstrates strong predictive performance. The LGB model shows lower variability but suffers from reduced predictive accuracy compared to the other two models. Overall, the CGB model emerges as the most reliable and accurate predictor for both Y1 and Y2.

4.3 | Uncertainty assessment

Figure 7 presents the estimated U_{95} metric in kN, which quantifies the uncertainty of predictions for the adopted models across both the training and testing stages for two outputs, Y1 and Y2. The U_{95} metric represents the 95% uncertainty interval, offering insights into the variability

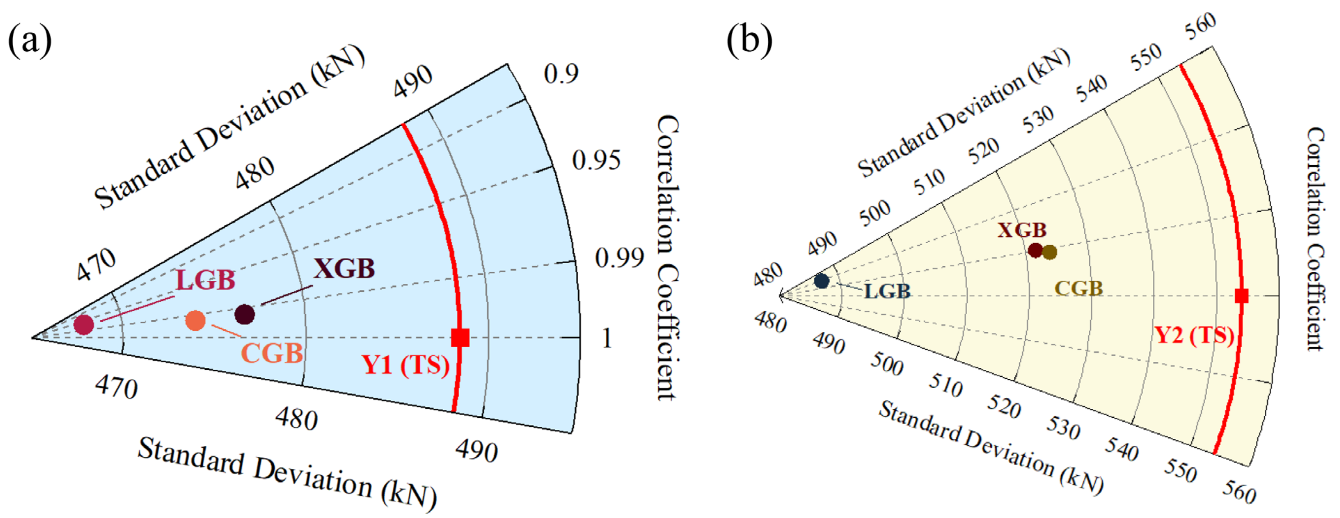

FIGURE 6 Taylor diagrams during the testing phase for (a) Y1 and (b) Y2.

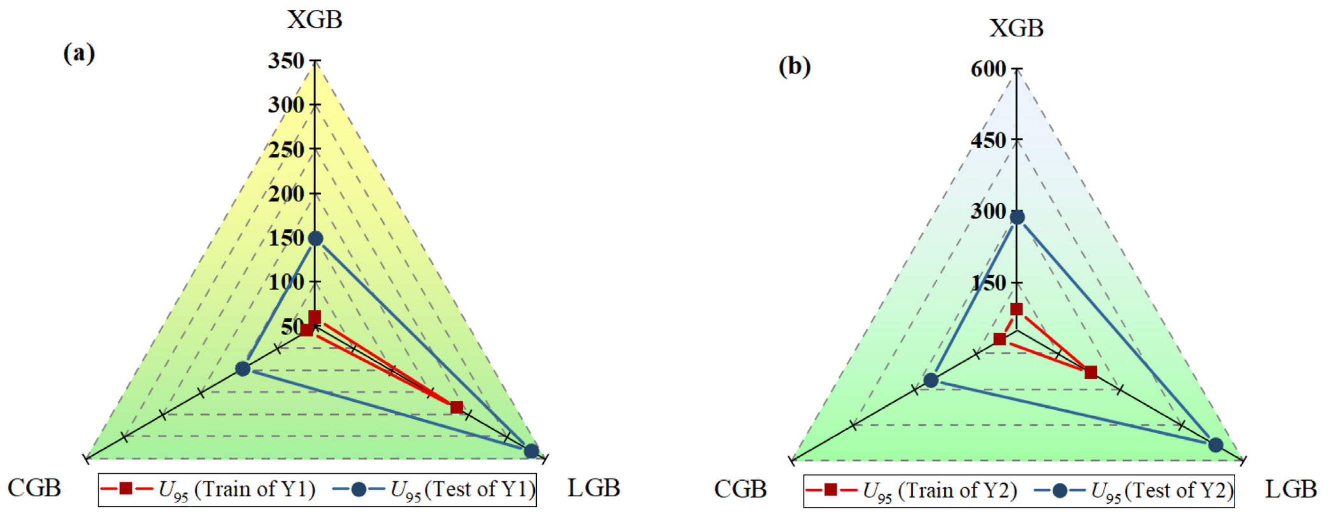

FIGURE 7 Estimated U_{95} metric in kN for checking the uncertainty of the predictions from the adopted models across both the training and testing stages (a) Y1 and (b) Y2.

and reliability of each model's predictions. For output Y1 during the training stage (Figure 7a), XGBoost and CatBoost demonstrate comparable U_{95} values of 59.296 and 60.321 kN, respectively, indicating low variability and high consistency in predictions. LightGBM, on the other hand, exhibits a significantly higher U_{95} value of 235.476 kN, suggesting greater uncertainty and less stable predictions during the training phase. In the testing stage for Y1, CatBoost achieves the lowest U_{95} value of 145.05 kN, followed closely by XGBoost at 149.625 kN, reflecting their strong generalization capabilities to unseen data. LightGBM shows a much higher U_{95} value of 331.948 kN, indicating greater variability and reduced reliability in its predictions during testing. For output, Y2 (Figure 7b), a similar pattern is observed. During the training stage, XGBoost and CatBoost show low U_{95} values of 91.773 and 91.215 kN, respectively, demonstrating minimal uncertainty and high consistency. LightGBM, with a U_{95} value of 230.633 kN, displays significantly higher uncertainty during the training phase. In the testing stage for Y2, CatBoost achieves the lowest U_{95} value of 260.041 kN, outperforming XGBoost, which has a U_{95} value of 288.125 kN. LightGBM, with a U_{95} value of 532.536 kN, exhibits the highest uncertainty, indicating considerable variability and less reliable predictions in testing.

The analysis of U_{95} values across both outputs and stages highlights the superior performance of CatBoost and XGBoost in maintaining lower uncertainty levels, particularly in the testing phase, where generalization is critical. LightGBM consistently shows higher U_{95} values, indicating greater variability and less reliable predictions compared to the other models. These findings underscore the robustness and reliability of CatBoost and XGBoost in capturing both outputs with minimal prediction uncertainty, making them more suitable for applications requiring accurate and consistent predictions.

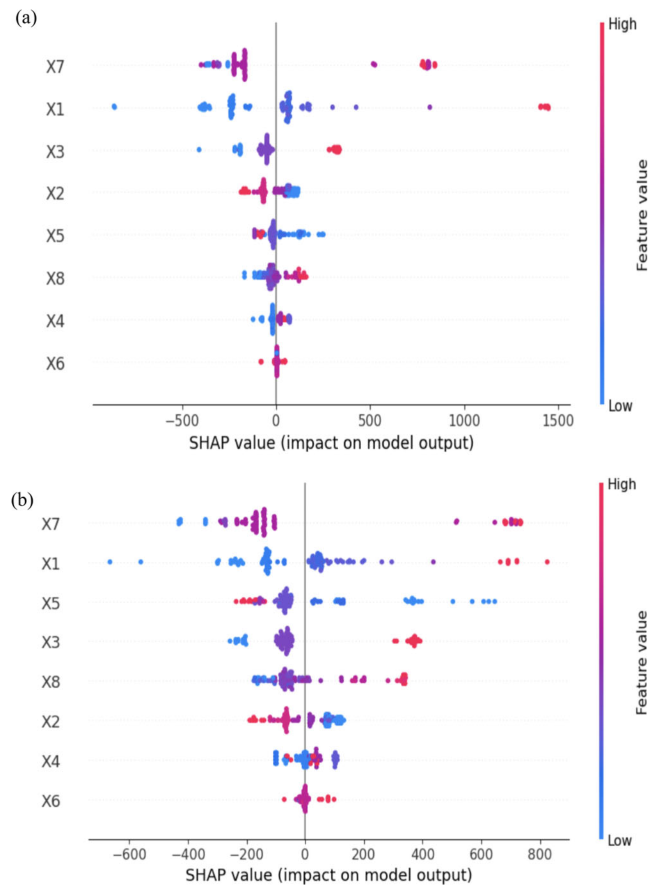

FIGURE 8 SHAP summary plots based on the CGB model for (a) Y1 and (b) Y2.

4.4 | Feature importance and interpretability analysis

4.4.1 | SHAP analysis

Figure 8 shows the SHAP summary plots illustrating the effect of the inputs on the prediction of a target variable of the two outputs based on the best predictive model, that is, the CGB model in both training and testing stages. In Figure 8a, X7 is identified as having the most significant impact on the prediction, with higher values of X7 generally increasing the model output, as shown by the red points on the right side of the plot. Following X7, X1 also exhibits a strong influence on the prediction. Features X3 and X2 also have substantial impacts, though they display mixed effects where both high and low values can significantly influence the prediction. Further down the list, X5, X8, X4, and X6 have relatively lesser impacts than the top features. Among these, X6 has the least influence on the model's output. Figure 8b shows that it is evident that feature X7 has the highest impact on the prediction, with both high and low values significantly influencing the model's output. X1 follows as the next most important feature, showing a range of SHAP values predominantly on the positive side, indicating that higher values of X1 generally increase the model's output. X5 is the third most influential feature, with a mix of high and low values substantially affecting the prediction. Features X3 and X8 also show significant impacts, with X3 having a balanced spread of SHAP values around zero and X8 showing a similar distribution with slightly more influence on the positive side. Lower down the list, X2 shows a varied impact with a notable spread of SHAP values, suggesting it has a moderate but consistent influence on the prediction. X4 and X6 have the least impact among the listed features, with X4 showing a more centralized distribution of SHAP values around zero, indicating a minimal effect on the prediction, and X6 displaying the least variance, suggesting it has the least influence on the model's output.

4.4.2 | PDP analysis

Figure 9 shows PDPs for the eight input variables (X1 to X8) against two outputs, Y1 and Y2. In Figure 9a, which

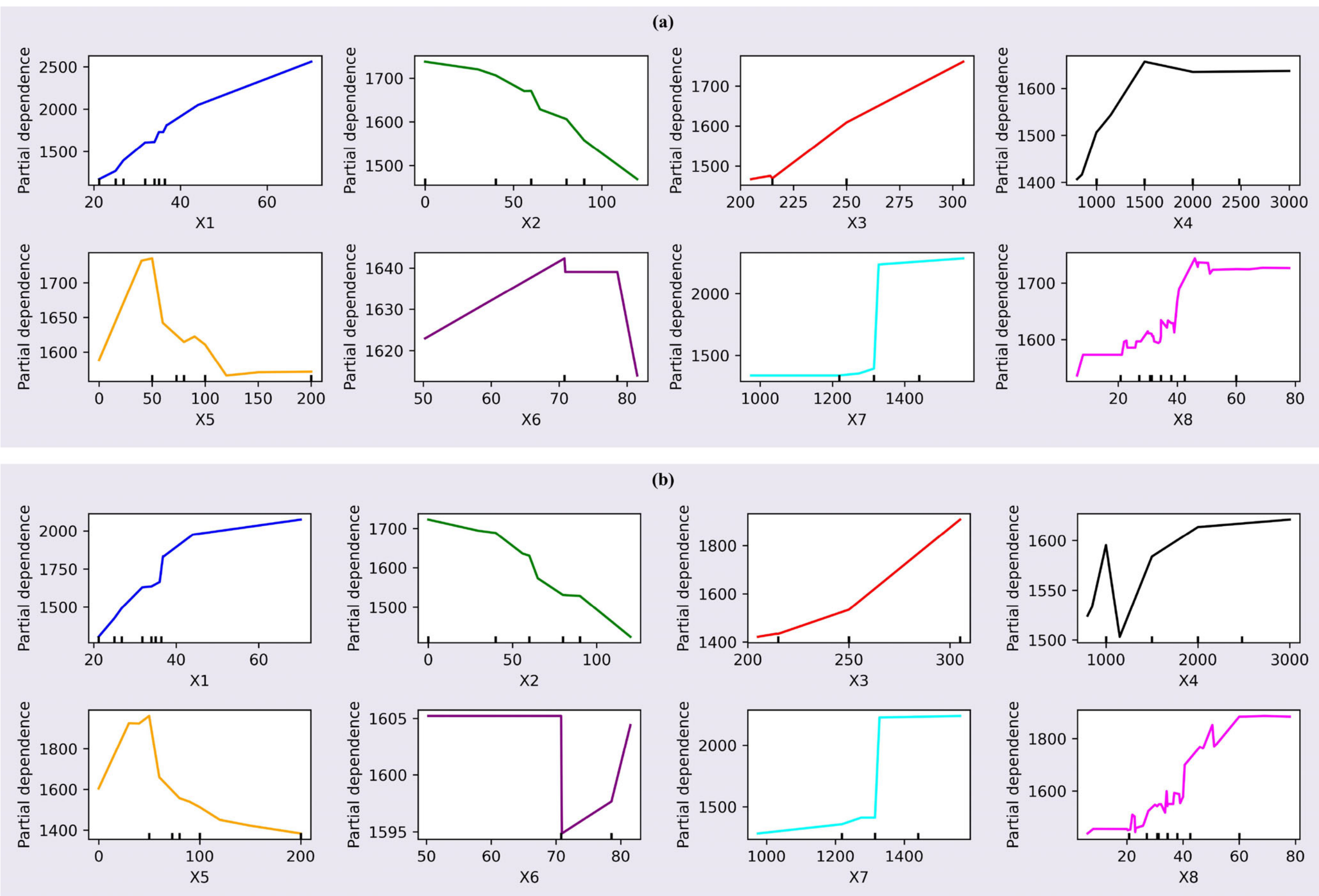

FIGURE 9 PDPs for each input feature based on the CGB model for (a) Y1 and (b) Y2.

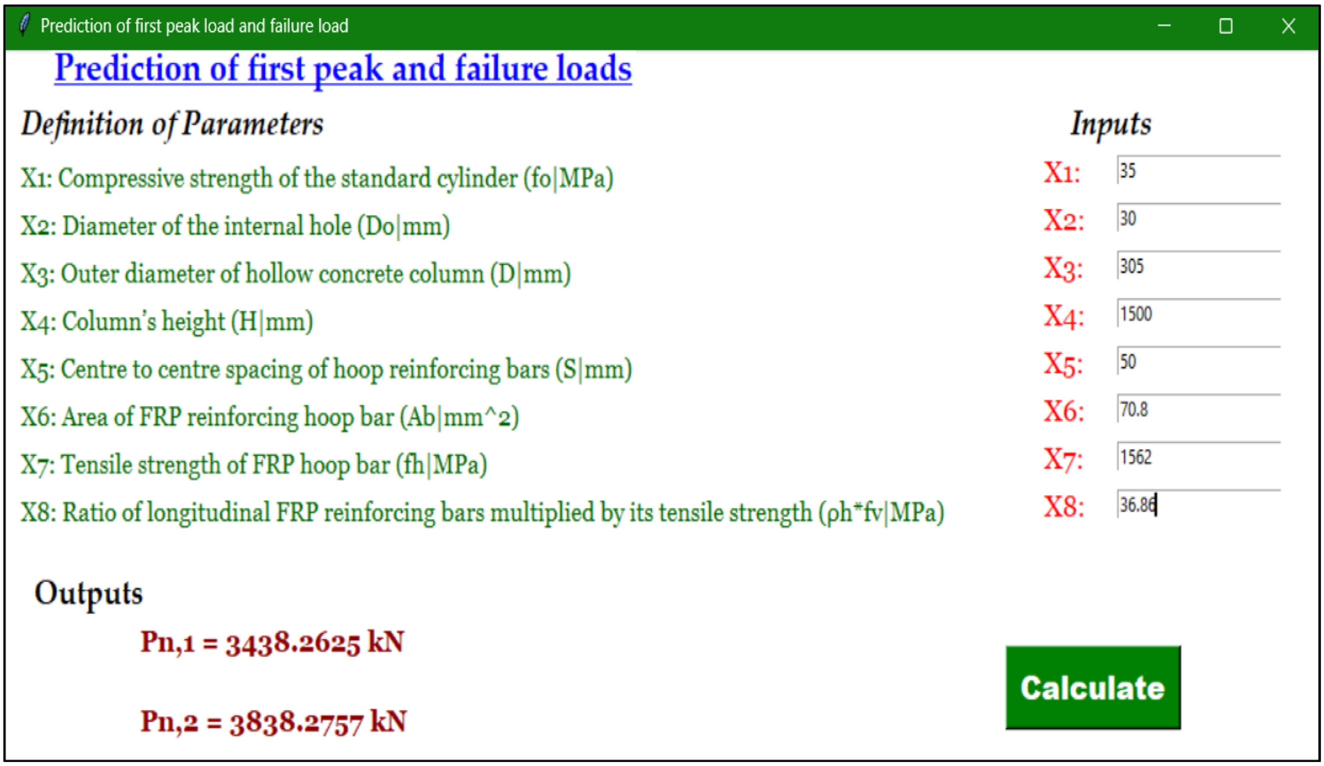

FIGURE 10 GUI screenshot for predicting Y1 and Y2.

corresponds to Y1, distinct patterns are observed for each input variable. For X1, a clear positive relationship exists, with increasing values of X1 leading to a steady rise in the partial dependence of Y1, indicating that higher values of X1 positively influence Y1. A similar trend is observed for X3, where Y1 increases linearly as X3 increases. X2, however, exhibits a negative relationship, where higher values of X2 correspond to a decrease in Y1, suggesting an inverse influence. X4 shows a nonlinear pattern, with a sharp increase in Y1 followed by a plateau, indicating a threshold effect. For X5, the partial dependence fluctuates significantly, suggesting a complex and possibly non-monotonic relationship with Y1. X6 shows a relatively stable and slightly positive trend, while X7 presents a distinct step-like pattern, indicating a sudden change in Y1 at specific values of X7. X8 demonstrates a jagged upward trend, suggesting a somewhat irregular but overall positive influence on Y1.

Figure 9b, which corresponds to Y2, shares some similarities with the trends observed in Y1 but also displays distinct differences. For X1, the relationship remains positive and linear, indicating that higher values of X1 consistently lead to an increase in Y2. X3 again shows a strong linear positive relationship, while X2 retains its negative association with Y2, reflecting its inverse influence. X4 exhibits a nonlinear and fluctuating pattern, with Y2 increasing sharply in some regions and stabilizing in others, indicating a complex interaction. X5 continues to show significant variability, suggesting a non-monotonic influence on Y2. X6 demonstrates a steeper change compared to Y1, indicating a more pronounced effect on Y2 at specific ranges. X7 retains its step-like behavior, with sharp increases in Y2 at certain values, suggesting the presence of thresholds or categorical effects. X8 displays a more prominent upward trend with fluctuations, indicating a stronger but somewhat irregular positive relationship with Y2. Overall, the PDPs highlight the differing contributions of the input variables to the two outputs, Y1 and Y2. Variables such as X1 and X3 consistently exhibit strong positive linear relationships across both outputs, while X2 consistently shows an inverse influence.

4.5 | Interactive GUI

This section presents a significant advancement to meet the practical needs of engineers and designers in efficiently utilizing ML models.[62] Although the complex processes of database assembly, model training, and validation have traditionally impeded the seamless integration of ML into everyday design tasks, an innovative solution has been developed. A Python web application has been created featuring a model with optimized hyperparameters accessible through an intuitive GUI built with the Tkinter package.[63] This GUI is specifically designed to predict outputs, as shown in Figure 10. The GUI presents a streamlined layout where users can enter values for the input variables. Upon inputting these variables, both calculated outputs are dynamically displayed, thereby providing immediate and tangible insights into the structural capacity of the column under consideration. To facilitate wider access and foster collaborative improvements, the GUI was and has been hosted on GitHub, making it readily available for use and further development by the community. This not only democratizes the use of advanced predictive models but also invites contributions to refine the tool and adapt it to various specific needs within the field of structural engineering. Finally, the GUI can be freely accessed at the following URL: https://github.com/mkamel24/PF.

5 | CONCLUSIONS

This study investigates the behavior of FRP-reinforced HCC using advanced ML models, including XGB, LGB, and CGB. The influence of eight key input parameters (f_o (X1), D_o (X2), D (X3), H (X4), S' (X5), A_b (X6), f_h (X7), $\rho_v f_v$ (X8)) on two critical outputs, the first peak load ($P_{n,1}$ (Y1)) and failure load $P_{n,2}$ (Y2) was analyzed. Prediction models were developed to assess the optimal parameter values and the structural performance of the column, with particular focus on determining the optimal design of FRP-reinforced HCC. The following conclusions are drawn:

1. ML models demonstrated a high degree of accuracy in predicting both the first peak load (Y1) and failure load (Y2). The XGB and CGB models emerged as the most accurate predictors, with R^2 values of 1.0 and 0.99 for Y1 during training and testing, respectively. For Y2, XGB and CGB achieved R^2 values of 0.99 during training and 0.96–0.97 during testing, reflecting their robust generalization capabilities. The LGB model, while effective, exhibited higher variability and reduced consistency, with R^2 values of 0.94 and 0.87 for testing Y1 and Y2, respectively. This suggests that LGB's performance, though adequate, is less reliable on unseen data.
2. Visual assessments, including scatter plots and violin boxplots, reveal that the CGB model provides the closest alignment with actual TS for both outputs. Its balanced distribution and controlled variability make it the top-performing model. Quantitative evaluations, such as Taylor diagrams and REC curves, further confirm CGB's superior predictive accuracy and lower residual errors compared to XGB and LGB. The XGB model, though slightly less accurate than CGB, consistently ranks as a strong performer, particularly in capturing the variability in both Y1 and Y2. LGB, despite its lower consistency, demonstrates reasonable accuracy and remains a viable alternative for predictions when computational efficiency is prioritized.
3. Feature importance analysis using SHAP values identifies f_h (X7) and f_o (X1) as the most influential input parameters for both Y1 and Y2. SHAP analysis highlights the significant and consistent impact of these features, with higher values of X7 and X1 generally increasing the predicted outputs. Other features, such as D (X3), D_o (X2), and S' (X5), also show substantial influence but exhibit more varied effects depending on their ranges. Features like H (X4) and A_b (X6) are identified as having minimal influence on the outputs, contributing less to the model's predictions.
4. PDPs provide further insights into the relationships between input features and outputs. A strong positive linear relationship is observed for X1 and X3 with both Y1 and Y2, indicating that increasing these variables leads to higher output values. Conversely, X2 consistently shows an inverse relationship, highlighting its negative contribution to both outputs.
5. A user-friendly GUI was developed to apply the CGB model for predicting Y1 and Y2, allowing engineers to input parameters and obtain instant predictions. It ensures accessibility by hosting on GitHub that supports collaborative improvements and enhances the practical application of ML models in structural design.

This study highlights the strong predictive capabilities of ML models, particularly CGB and XGB, for FRP-reinforced HCC, despite limitations such as a relatively small dataset and limited exploration of multicollinearity among inputs. These models demonstrate exceptional accuracy and reliability within these constraints. Future work should focus on expanding datasets and incorporating additional environmental factors to enhance generalizability. Exploring hybrid modeling approaches that integrate physical models with ML could further refine prediction accuracy and adaptability for diverse engineering applications.

AUTHOR CONTRIBUTIONS

Conceptualization, *Project administration*, *Supervision*, *Funding acquisition*: H.F.I., W.J.K.A. *Conceptualization*, *Formal analysis*, *Investigation*, *Visualization*, *Methodology*, *Validation*, *Writing—original draft*, *Visualization*, *Software*, *Resources*, *Data curation*, *Writing–review and editing*: J.Z., W.J.K.A., H.F.I., B.S.N., H.A.M., M.E.K. All authors have read and agreed to the published version of the manuscript.

ACKNOWLEDGMENTS

The authors extend their appreciation to King Saud University for funding this work through Researchers Supporting Project number (RSPD2025R1006), King Saud University, Riyadh, Saudi Arabia.

FUNDING INFORMATION

This research received no external funding.

CONFLICT OF INTEREST STATEMENT

The authors declared that no competing interests exist.

DATA AVAILABILITY STATEMENT

The data that support the findings of this study are available from the corresponding author upon reasonable request.

ORCID

Jie Zhang https://orcid.org/0009-0009-3507-3713
Haytham F. Isleem https://orcid.org/0000-0002-4826-7420
Bichitra Singh Negi https://orcid.org/0000-0002-3142-0062
Mohamed Kamel Elshaarawy https://orcid.org/0000-0002-1793-5617

REFERENCES

1. Lu D, Zhou X, Du X, Wang G. A 3D fractional elastoplastic constitutive model for concrete material. Int J Solids Struct. 2019;165:160–75.
2. Isleem HF, Zewudie BB, Bahrami A, Kumar R, Xingchong W, Samui P. Parametric investigation of rectangular CFRP-confined concrete columns reinforced by inner elliptical steel tubes using finite element and machine learning models. Heliyon. 2024;10(2):e23666.
3. Lignola GP, Nardone F, Prota A, De Luca A, Nanni A. Analysis of RC hollow columns strengthened with GFRP. J Compos Constr. 2011;15:545–56.
4. Cassese P, De Risi MT, Verderame GM. Seismic assessment of existing hollow circular reinforced concrete bridge piers. J Earthq Eng. 2020;24:1566–601.
5. AlAjarmeh OS, Manalo AC, Benmokrane B, Karunasena W, Mendis P, Nguyen KT. Compressive behavior of axially loaded circular hollow concrete columns reinforced with GFRP bars and spirals. Construct. Build Mater. 2019;194:12–23.
6. Hadi MNS, Ahmad H, Sheikh MN. Effect of using GFRP reinforcement on the behavior of hollow-core circular concrete columns. J Compos Constr. 2021;25(1):06020003.
7. Ephraim ME, Adetiloye A, Harcourt P. Mechanical properties of glass fibre reinforced polymer based on resin from recycled plastic. IJSER. 2015;6:145–52.
8. Jabbar SA, Farid SBH. Replacement of steel rebars by GFRP rebars in the concrete structures. Karbala Int J Mod Sci. 2018;4:216–27.
9. Isleem HF, Tayeh BA, Alaloul WS, Musarat MA, Raza A. Artificial neural network (ANN) and finite element (FEM) models for GFRP-reinforced concrete columns under axial compression. Materials. 2021;14:7172.
10. Isleem HF, Augustino DS, Mohammed AS, Najemalden AM, Jagadesh P, Qaidi S, et al. Finite element, analytical, artificial neural network models for carbon fibre reinforced polymer confined concrete filled steel columns with elliptical cross sections. Front. Mater. Sci. 2023a;9:1115394.
11. 440.1R-06. A. Guide for the Design and Construction of Structural Concrete Reinforced with FRP Bars. In (American Concrete Institute) 2006.
12. Afifi MZ, Mohamed HM, Benmokrane B. Theoretical stress–strain model for circular concrete columns confined by GFRP spirals and hoops. Eng Struct. 2015;102:202–13.
13. Isleem HF, Qiong T, Alsaadawi MM, Elshaarawy MK, Mansour DM, Abdullah F, et al. Numerical and machine learning modeling of GFRP confined concrete-steel hollow elliptical columns. Sci. Rep. 2024a;14(1):18647.
14. Isleem HF, Tayeh BA, Abid M, Iqbal M, Mohamed AM, Sherbiny MGE. Finite element and artificial neural network modeling of FRP-RC columns under axial compression loading. Front. Mater. Sci. 2022;9:1–27, 888909.
15. Tobbi H, Farghaly AS, Benmokrane B. Concrete columns reinforced longitudinally and transversally with glass fiber-reinforced polymer bars. ACI Struct J. 2012;109:551–8.
16. Barua S, El-Salakawy E. Performance of GFRP-reinforced concrete circular short columns under concentric, eccentric, and flexural loads. J. Compos. Constr. 2020;24(5):04020044.
17. Zeng J-J, Feng P, Dai J-G, Zhuge Y. Development and behavior of novel FRP-UHPC tubular members. Eng Struct. 2022;266:114540.
18. Ye Y-Y, Zhuge Y, Smith ST, Zeng J-J, Bai Y-L. Behavior of GFRP-RC columns under axial compression: Assessment of existing models and a new axial load-strain model. J Build Eng. 2022;47:103782.
19. Feng G, Zhu D, Guo S, Rahman MZ, Jin Z, Shi C. A review on mechanical properties and deterioration mechanisms of FRP bars under severe environmental and loading conditions. Cem Concr Compos. 2022;134:104758.
20. Pantelides CP, Gibbons ME, Reaveley LD. Axial load behavior of concrete columns confined with GFRP Spirals. J Compos Constr. 2013;17:305–13.
21. Isleem HF, Chukka NDKR, Bahrami A, Oyebisi S, Kumar R, Qiong T. Nonlinear finite element and analytical modelling of reinforced concrete filled steel tube columns under axial compression loading. Results in Engineering. 2023b;19:101341.
22. GB/T 30022-2013. Test Method for Basic Mechanical Properties of Fiber Reinforced Polymer Bar. Beijing, China [in Chinese]. 2013.
23. CSA Standards. Design and construction of building components with fibre-reinforced polymers. *S806-02*, Can. Stand. Assoc 2002.
24. Zhang C, Shu J, Zhang H, Ning Y, Yu Y. Estimation of load-carrying capacity of cracked RC beams using 3D digital twin model integrated with point clouds and images. Eng Struct. 2024;310:118126.
25. Liao J, Zeng J-J, Jiang C, Li J-X, Yuan J-S. Stress-strain behavior and design-oriented model for FRP spiral strip-confined concrete. Compos Struct. 2022;293:115747.

26. Zeng Y, Xu L, Chi Y, Yu M, Huang L. Compressive behavior of circular GFRP tube-confined UHPC-filled steel-encased stub columns. Compos Struct. 2023;309:116730.
27. Huang H, Guo M, Zhang W, Zeng J, Yang K, Bai H. Numerical investigation on the bearing capacity of RC columns strengthened by HPFL-BSP under combined loadings. J. Build. Eng. 2021;39:102266.
28. Guo M, Huang H, Zhang W, Xue C, Huang M. Assessment of RC frame capacity subjected to a loss of corner column. J. Struct. Eng. 2022;148(9):04022122.
29. Karimipour A, Abad JMN, Fasihihour N. Predicting the load-carrying capacity of GFRP-reinforced concrete columns using ANN and evolutionary strategy. Compos Struct. 2021;275:114470.
30. Long X, Li H, Iyela PM, Kang S. Predicting the bond stress?slip behavior of steel reinforcement in concrete under static and dynamic loadings by finite element, deep learning and analytical methods. Eng Fail Anal. 2024;161:108312.
31. Wang J, Han J, Zhu C, Lu W, Zhang Y, He X, et al. Structural optimization and engineering application of concrete-filled steel tubular composite supports. Eng. Fail. Anal. 2024;159:108082.
32. Asteris PG, Tsavdaridis KD, Lemonis ME, Ferreira FPV, Le TT, Gantes CJ, et al. AI-powered GUI for prediction of axial compression capacity in concrete-filled steel tube columns. Neural Comput. Applic. 2024;36(35):22429–59.
33. Fatehi E, Yazdani Sarvestani H, Ashrafi B, Akbarzadeh AH. Accelerated design of architectured ceramics with tunable thermal resistance via a hybrid machine learning and finite element approach. Mater Des. 2021;210:110056.
34. Sakino K, Nakahara H, Morino S, Nishiyama I. Behavior of centrally loaded concrete-filled steel-tube short columns. J Struct Eng. 2004;130:180–8.
35. Yan F, Lin Z, Wang X, Azarmi F, Sobolev K. Evaluation and prediction of bond strength of GFRP-bar reinforced concrete using artificial neural network optimized with genetic algorithm. Compos Struct. 2017;161:441–52.
36. Aravind N, Nagajothi S, Elavenil S. Machine learning model for predicting the crack detection and pattern recognition of geopolymer concrete beams. Constr Build Mater. 2021;297:123785.
37. Bakouregui AS, Mohamed HM, Yahia A, Benmokrane B. Explainable extreme gradient boosting tree-based prediction of load-carrying capacity of FRP-RC columns. Eng Struct. 2021;245:112836.
38. Basaran B, Kalkan I, Bergil E, Erdal E. Estimation of the FRP-concrete bond strength with code formulations and machine learning algorithms. Compos Struct. 2021;268:113972.
39. Fallah Madvari R. Artificial Intelligence (AI), Machine Learning (ML) and Deep Learning (DL) on Health, Safety and Environment (HSE). Arch Occup Health. 2022;6(4):1321–2.
40. Alzubi J, Nayyar A, Kumar A. Machine learning from theory to algorithms: an overview. J Phys: Conf Ser. 2018;1142:12012.
41. Elshaarawy MK, Hamed AK. Stacked ensemble model for optimized prediction of triangular side orifice discharge coefficient. Eng Optim. 2024;56. https://doi.org/10.1080/0305215X.2024.2397431
42. Elshaarawy MK, Alsaadawi MM, Hamed AK. Machine learning and interactive GUI for concrete compressive strength prediction. Sci Rep. 2024;14:16694.
43. Elshaarawy MK, Elmasry NH, Selim T, Elkiki M, Eltarabily MG. Determining seepage loss predictions in lined canals through optimizing advanced gradient boosting techniques. Water Conserv Sci Eng. 2024;9:75. https://doi.org/10.1007/s41101-024-00306-3
44. Kabeel AE, Elazab MA, El Hadi Attia M, Elshaarawy MK, Hamed AK, Alsaadawi MM, et al. Exploring the potential of conical solar stills: design optimization and enhanced performance overview. Desalin. Water Treat. 2024;320:100642. https://doi.org/10.1016/j.dwt.2024.100642
45. Eltarabily MG, Elshaarawy MK. Risk assessment of potential groundwater contamination by agricultural drainage water in the central Valley Watershed, California, USA. Groundwater Quality and Geochemistry in Arid and Semi-Arid Regions. Cham: Springer Nature Switzerland; 2023. p. 37–76.
46. Chen T, Guestrin C. XGBoost. Proceedings of the 22nd ACM SIGKDD International Conference on Knowledge Discovery and Data Mining. San Francisco, CA: ACM; 2016. p. 785–94. https://doi.org/10.1145/2939672.2939785
47. Eltarabily MG, Abd-Elhamid HF, Zeleňáková M, Elshaarawy MK, Elkiki M, Selim T. Predicting seepage losses from lined irrigation canals using machine learning models. Front. water. 2023;5:1287357.
48. Wang D, Zhang Y, Zhao Y. LightGBM: an effective miRNA classification method in breast cancer patients. Proceedings of the 2017 International Conference on Computational Biology and Bioinformatics. New York, NY: Association for Computing Machinery; 2017. p. 7–11.
49. Yan J, Xu Y, Cheng Q, Jiang S, Wang Q, Xiao Y, et al. LightGBM: accelerated genomically designed crop breeding through ensemble learning. Genome Biol. 2021;22:1–24.
50. Dorogush AV, Ershov V, Gulin A. CatBoost: gradient boosting with categorical features support. arXiv1810.11363 2018 https://doi.org/10.48550/arXiv.1810.11363
51. Elshaarawy MK, Hamed AK. Predicting discharge coefficient of triangular side orifice using ANN and GEP models. Water Sci. 2024;38:1–20.
52. Elshaarawy M, Hamed AK, Hamed S. Regression-based models for predicting discharge coefficient of triangular side orifice. J Eng Res. 2023;7:224–31.
53. Benzaamia A, Ghrici M, Rebouh R, Zygouris N, Asteris PG. Predicting the shear strength of rectangular RC beams strengthened with externally-bonded FRP composites using constrained monotonic neural networks. Eng Struct. 2024;313:118192.
54. Luat N-V, Han SW, Lee K. Genetic algorithm hybridized with eXtreme gradient boosting to predict axial compressive capacity of CCFST columns. Compos Struct. 2021;278:114733.
55. Eltarabily MG, Elshaarawy MK, Elkiki M, Selim T. Modeling surface water and groundwater interactions for seepage losses estimation from unlined and lined canals. Water Sci. 2023;37:315–28.
56. Eltarabily MG, Elshaarawy MK, Elkiki M, Selim T. Computational fluid dynamics and artificial neural networks for modelling lined irrigation canals with low-density polyethylene and cement concrete liners. Irrig Drain. 2024;73:910–27.
57. Isleem HF, Elshaarawy MK, Hamed AK. Analysis of flow dynamics and energy dissipation in piano key and labyrinth weirs using computational fluid dynamics. Computational Fluid Dynamics—Analysis, Simulations, and Applications. London, UK: IntechOpen; 2024. https://doi.org/10.5772/intechopen.1006332
58. Eltarabily MG, Selim T, Elshaarawy MK, Mourad MH. Numerical and experimental modeling of geotextile soil reinforcement

for optimizing settlement and stability of loaded slopes of irrigation canals. Environ Earth Sci. 2024;83:246.

59. Selim T, Elshaarawy MK, Elkiki M, Eltarabily MG. Estimating seepage losses from lined irrigation canals using nonlinear regression and artificial neural network models. Appl Water Sci. 2024;14:90.
60. Tian W, Isleem HF, Hamed AK, Elshaarawy MK. Enhancing discharge prediction over type-A piano key weirs: An innovative machine learning approach. Flow Meas Instrum. 2024;100:102732.
61. Elshaarawy MK, Elkiki M, Selim T, Eltarabily MG. Hydraulic comparison of different types of lining for irrigation canals using computational fluid dynamic models. M.Sc. Thesis, 2024 https://doi.org/10.13140/RG.2.2.21927.97441.Civil Engineering Department, Faculty of Engineering, Port Said University
62. Elshaarawy MK, Eltarabily MG. Machine learning models for predicting water quality index: optimization and performance analysis for El Moghra, Egypt. Water Supply. 2024;24(9):3269–94. https://doi.org/10.2166/ws.2024.189
63. Pant A, Ramana GV. Prediction of pullout interaction coefficient of geogrids by extreme gradient boosting model. Geotext Geomembranes. 2022;50:1188–98.

AUTHOR BIOGRAPHIES

Jie Zhang was born in Xinxiang, Henan, P. R. China, in 1987. He was received the Master degree from School of Civil Engineering and Architecture, Henan University, China. He has been working in the field of construction engineering for 13 years. Now he is serving as a lecturer at the School of Mechanical and Electrical Engineering, Xinxiang University, China. His research expertise includes engineering management, artificial intelligence, intelligent construction, engineering materials, etc. Email: zhangjie2222@xxu.edu.cn.

Walaa J. K. Almoghayer School of business, Nanjing University of Information Science & Technology, Nanjing, China. Email: 202452250110@nuist.edu.cn.

Haytham F. Isleem Jadara Research Center, Jadara University, Irbid, Jordan; Department of computer Science, University of York, York, UK. Email: mps565@york.ac.uk; isleemhaytham88@gmail.com.

Bichitra Singh Negi Department of Civil Engineering, Dev Bhoomi Uttarakhand University, Dehradun, India. Email: ce.bichitra@dbuu.ac.in.

Haitham A. Mahmoud Industrial Engineering Department, College of Engineering, King Saud University, Riyadh, Saudi Arabia. Email: hmahmoud@ksu.edu.sa.

Mohamed Kamel Elshaarawy Assistant Lecturer in the Civil Engineering Department at the Faculty of Engineering, Horus University-Egypt, in New Damietta. Email: melshaarawy@horus.edu.eg; mohamed.elshaarawy@eng.psu.edu.eg.

How to cite this article: Zhang J, Almoghayer WJK, Isleem HF, Negi BS, Mahmoud HA, Elshaarawy MK. Machine learning for the prediction of the axial load-carrying capacity of FRP reinforced hollow concrete column. Structural Concrete. 2025. https://doi.org/10.1002/suco.202400886

APPENDIX A

TABLE A1 Database of the input parameters and their actual and predicted outputs.

S. no.	X1 f_o (MPa)	X2 D_o (mm)	X3 D (mm)	X4 H (mm)	X5 S' (mm)	X6 A_b (mm^2)	X7 f_h (MPa)	X8 $\rho_v \times f_v$ (MPa)	Y1 $P_{n,1}$ (kN)	Predicted Y1	Y2 $P_{n,2}$ (kN)	Predicted Y2
1	21.20	120.00	250.00	2000.00	100.00	70.80	1315.00	38.98	842.01	**839.31**	888.33	**888.57**
2	25.00	120.00	250.00	1000.00	100.00	70.80	1315.00	25.76	905.54	**907.15**	827.58	**828.15**
3	21.20	90.00	250.00	1000.00	100.00	70.80	1315.00	34.47	907.00	**926.97**	849.00	**925.75**
4	21.20	90.00	250.00	2000.00	200.00	70.80	1315.00	30.79	908.05	**908.22**	906.88	**906.33**
5	25.00	120.00	250.00	1000.00	100.00	70.80	1315.00	26.00	910.01	**909.28**	830.15	**844.86**
6	21.20	90.00	250.00	2000.00	100.00	70.80	1315.00	34.47	930.06	**931.13**	1000.16	**983.53**
7	21.20	90.00	250.00	1000.00	100.00	70.80	1315.00	34.47	942.63	**926.97**	1001.61	**925.75**
8	34.00	0.00	215.00	1150.00	120.00	50.29	975.00	6.04	943.00	**989.45**	707.25	**749.98**
9	21.20	65.00	250.00	2000.00	100.00	70.80	1315.00	32.18	968.54	**972.13**	1036.98	**1038.18**
10	36.00	90.00	214.00	850.00	60.00	78.57	1219.00	26.17	980.35	**1022.64**	942.05	**1043.78**
11	36.00	90.00	214.00	850.00	90.00	78.57	1219.00	26.17	982.10	**980.65**	901.77	**902.56**
12	25.00	90.00	250.00	1000.00	100.00	70.80	1315.00	22.99	983.30	**1015.82**	875.50	**923.57**
13	25.00	120.00	250.00	1000.00	100.00	70.80	1315.00	38.64	984.69	**985.99**	969.38	**969.94**
14	25.00	120.00	250.00	1000.00	100.00	70.80	1315.00	39.00	995.06	**956.97**	973.14	**945.22**
15	21.20	40.00	250.00	2000.00	200.00	70.80	1315.00	30.79	1006.65	**1017.52**	989.54	**1031.91**
16	25.00	90.00	250.00	1000.00	100.00	70.80	1315.00	22.77	1011.17	**1034.75**	919.94	**983.57**
17	25.00	90.00	250.00	1000.00	100.00	70.80	1315.00	22.99	1015.58	**1015.82**	922.00	**923.57**
18	21.20	0.00	250.00	2000.00	200.00	70.80	1315.00	30.00	1020.60	**1038.18**	990.90	**1011.83**
19	26.80	90.00	250.00	1000.00	0.00	70.80	1315.00	34.47	1022.00	**1020.78**	854.65	**855.04**
20	21.20	90.00	250.00	3000.00	50.00	70.80	1315.00	34.47	1028.02	**1060.37**	1251.85	**1286.54**
21	34.00	0.00	215.00	1150.00	120.00	50.29	975.00	8.05	1031.00	**1046.24**	773.25	**770.18**
22	21.20	120.00	250.00	2000.00	100.00	70.80	1315.00	77.97	1034.53	**1032.12**	1388.63	**1387.65**
23	25.00	90.00	250.00	1000.00	100.00	70.80	1315.00	34.16	1035.00	**1054.81**	1204.20	**1141.01**
24	25.00	90.00	250.00	1000.00	100.00	70.80	1315.00	22.77	1035.30	**1034.75**	985.10	**983.57**
25	34.00	0.00	215.00	1150.00	120.00	50.29	975.00	6.04	1039.25	**989.45**	791.70	**749.98**
26	21.20	40.00	250.00	2000.00	100.00	70.80	1315.00	30.79	1044.34	**1036.45**	1149.99	**1148.53**
27	34.00	0.00	215.00	1150.00	120.00	50.29	975.00	8.05	1052.04	**1046.24**	768.10	**770.18**
28	26.80	90.00	250.00	1000.00	0.00	70.80	1315.00	34.47	1055.52	**1020.78**	926.22	**855.04**
29	36.00	56.00	214.00	850.00	90.00	78.57	1219.00	23.13	1061.00	**1079.33**	845.00	**927.84**
30	25.00	90.00	250.00	1000.00	100.00	70.80	1315.00	34.16	1067.16	**1054.81**	1078.70	**1141.01**
31	25.00	120.00	250.00	1000.00	100.00	70.80	1315.00	51.99	1067.21	**1064.73**	1139.57	**1139.44**
32	34.00	0.00	215.00	1150.00	80.00	50.29	975.00	8.05	1068.85	**1076.11**	853.22	**840.42**
33	21.20	0.00	250.00	2000.00	100.00	70.80	1315.00	30.00	1073.88	**1070.06**	1167.07	**1182.24**
34	25.00	60.00	250.00	1000.00	100.00	70.80	1315.00	21.03	1079.79	**1083.86**	993.99	**996.75**
35	21.20	90.00	250.00	2000.00	200.00	70.80	1315.00	68.94	1083.26	**1110.81**	1384.68	**1393.04**
36	25.00	60.00	250.00	1000.00	100.00	70.80	1315.00	21.23	1083.94	**1083.86**	996.03	**996.75**
37	34.00	0.00	215.00	1150.00	80.00	50.29	975.00	8.05	1088.00	**1076.11**	828.03	**840.42**
38	36.00	56.00	214.00	850.00	60.00	78.57	1219.00	23.13	1088.00	**1127.84**	1199.00	**1109.45**

TABLE A1 (Continued)

S. no.	X1 f_o (MPa)	X2 D_o (mm)	X3 D (mm)	X4 H (mm)	X5 S' (mm)	X6 A_b (mm^2)	X7 f_h (MPa)	X8 $\rho_v \times f_v$ (MPa)	Y1 $P_{n,1}$ (kN)	Predicted Y1	Y2 $P_{n,2}$ (kN)	Predicted Y2
39	21.20	65.00	250.00	3000.00	50.00	70.80	1315.00	32.18	1092.89	**1091.14**	1357.01	**1356.64**
40	25.00	90.00	250.00	1000.00	100.00	70.80	1315.00	34.48	1097.93	**1101.25**	1081.41	**1052.39**
41	36.00	56.00	214.00	850.00	90.00	78.57	1219.00	23.13	1098.62	**1079.33**	1011.89	**927.84**
42	26.80	90.00	250.00	1000.00	150.00	70.80	1315.00	34.47	1108.00	**1123.39**	1110.00	**1027.85**
43	25.00	90.00	250.00	1000.00	100.00	70.80	1315.00	34.48	1109.20	**1101.25**	1024.40	**1052.39**
44	25.00	120.00	250.00	1000.00	100.00	70.80	1315.00	57.77	1118.42	**1092.30**	1208.21	**1313.10**
45	36.00	56.00	214.00	850.00	60.00	78.57	1219.00	23.13	1119.64	**1127.84**	1107.67	**1109.45**
46	25.00	30.00	250.00	1000.00	100.00	70.80	1315.00	20.11	1120.06	**1125.98**	1039.45	**1044.29**
47	21.20	90.00	250.00	2000.00	100.00	70.80	1315.00	68.94	1121.80	**1119.43**	1498.20	**1498.85**
48	26.80	90.00	250.00	1000.00	150.00	70.80	1315.00	34.47	1122.21	**1123.39**	1027.95	**1027.85**
49	25.00	30.00	250.00	1000.00	100.00	70.80	1315.00	20.30	1123.45	**1125.98**	1040.37	**1039.63**
50	25.00	90.00	250.00	1000.00	100.00	70.80	1315.00	51.08	1140.00	**1145.04**	1247.90	**1249.04**
51	31.80	120.00	250.00	2000.00	200.00	70.80	1315.00	38.98	1146.80	**1147.16**	1004.77	**1006.79**
52	36.00	56.00	214.00	850.00	30.00	78.57	1219.00	23.13	1154.00	**1283.95**	1955.00	**1641.06**
53	26.80	90.00	250.00	1000.00	100.00	70.80	1315.00	34.47	1157.38	**1166.70**	1117.34	**1111.90**
54	36.00	30.00	214.00	850.00	90.00	78.57	1219.00	21.98	1157.79	**1135.96**	1082.48	**1028.33**
55	21.20	40.00	250.00	2000.00	200.00	70.80	1315.00	61.58	1160.46	**1188.86**	1437.25	**1467.57**
56	21.20	65.00	250.00	2000.00	100.00	70.80	1315.00	64.35	1160.74	**1163.92**	1539.08	**1539.31**
57	25.00	60.00	250.00	1000.00	100.00	70.80	1315.00	31.55	1162.79	**1161.70**	1151.77	**1151.65**
58	26.80	90.00	250.00	1000.00	50.00	70.80	1315.00	34.47	1163.39	**1205.90**	1386.62	**1432.05**
59	25.00	60.00	250.00	1000.00	100.00	70.80	1315.00	31.85	1167.48	**1161.70**	1153.13	**1151.65**
60	31.80	120.00	250.00	2000.00	100.00	70.80	1315.00	38.98	1168.57	**1168.81**	1092.02	**1088.60**
61	25.00	0.00	250.00	1000.00	100.00	70.80	1315.00	20.11	1169.99	**1168.05**	1108.40	**1109.12**
62	25.00	0.00	250.00	1000.00	100.00	70.80	1315.00	20.30	1173.78	**1168.05**	1109.50	**1104.46**
63	25.00	90.00	250.00	1000.00	100.00	70.80	1315.00	45.97	1176.34	**1217.29**	1247.95	**1326.45**
64	37.00	0.00	205.00	800.00	60.00	70.91	1275.00	27.63	1180.23	**1181.79**	1358.40	**1358.28**
65	34.00	0.00	215.00	1150.00	40.00	50.29	975.00	8.05	1180.46	**1201.60**	1154.32	**1151.42**
66	21.20	40.00	250.00	3000.00	50.00	70.80	1315.00	30.79	1183.25	**1179.49**	1500.46	**1500.98**
67	26.80	90.00	250.00	1000.00	100.00	70.80	1315.00	34.47	1189.00	**1166.70**	1102.00	**1111.90**
68	21.20	0.00	250.00	3000.00	50.00	70.80	1315.00	30.00	1196.09	**1200.42**	1545.98	**1546.54**
69	26.80	90.00	250.00	1000.00	50.00	70.80	1315.00	34.47	1197.00	**1205.90**	1434.00	**1432.05**
70	25.00	90.00	250.00	1000.00	100.00	70.80	1315.00	51.08	1199.24	**1145.04**	1318.59	**1249.04**
71	25.00	30.00	250.00	1000.00	100.00	70.80	1315.00	30.17	1203.13	**1208.22**	1195.82	**1194.94**
72	21.20	0.00	250.00	2000.00	200.00	70.80	1315.00	60.00	1203.42	**1199.33**	1437.25	**1438.39**
73	36.00	30.00	214.00	850.00	60.00	78.57	1219.00	21.98	1204.69	**1200.11**	1234.19	**1233.69**
74	25.00	30.00	250.00	1000.00	100.00	70.80	1315.00	30.45	1207.03	**1208.22**	1196.12	**1194.94**
75	37.00	0.00	205.00	800.00	60.00	70.91	1275.00	27.63	1220.00	**1181.79**	1425.00	**1358.28**
76	34.00	0.00	215.00	1150.00	40.00	50.29	975.00	8.05	1223.00	**1201.60**	1147.75	**1151.42**
77	21.20	40.00	250.00	2000.00	100.00	70.80	1315.00	61.58	1236.13	**1235.99**	1646.71	**1638.10**
78	25.00	60.00	250.00	1000.00	100.00	70.80	1315.00	42.46	1247.75	**1256.04**	1319.06	**1327.59**
79	25.00	0.00	250.00	1000.00	100.00	70.80	1315.00	30.17	1250.05	**1244.79**	1260.45	**1260.24**

(Continues)

TABLE A1 (Continued)

S. no.	X1 f_o (MPa)	X2 D_o (mm)	X3 D (mm)	X4 H (mm)	X5 S' (mm)	X6 A_b (mm^2)	X7 f_h (MPa)	X8 $\rho_v \times f_v$ (MPa)	Y1 $P_{n,1}$ (kN)	Predicted Y1	Y2 $P_{n,2}$ (kN)	Predicted Y2
80	21.20	0.00	250.00	2000.00	100.00	70.80	1315.00	60.00	1250.52	**1259.40**	1657.18	**1655.45**
81	25.00	0.00	250.00	1000.00	100.00	70.80	1315.00	30.45	1256.61	**1244.79**	1265.49	**1260.24**
82	31.80	90.00	250.00	2000.00	200.00	70.80	1315.00	34.47	1264.64	**1265.01**	1102.49	**1099.25**
83	25.00	90.00	250.00	1000.00	100.00	70.80	1315.00	45.97	1267.90	**1217.29**	1406.10	**1326.45**
84	36.00	56.00	214.00	850.00	30.00	78.57	1219.00	23.13	1285.91	**1283.95**	1641.72	**1641.06**
85	25.00	30.00	250.00	1000.00	100.00	70.80	1315.00	40.60	1288.20	**1297.64**	1362.01	**1364.70**
86	37.00	0.00	205.00	800.00	30.00	70.91	1275.00	27.63	1291.10	**1324.54**	1939.07	**1743.31**
87	25.00	60.00	250.00	1000.00	100.00	70.80	1315.00	47.17	1293.23	**1297.01**	1386.45	**1386.50**
88	31.80	90.00	250.00	2000.00	100.00	70.80	1315.00	34.47	1294.41	**1311.35**	1194.20	**1201.42**
89	37.00	0.00	205.00	800.00	30.00	70.91	1275.00	27.63	1309.00	**1324.54**	2041.00	**1743.31**
90	31.80	65.00	250.00	2000.00	200.00	70.80	1315.00	32.18	1325.91	**1320.45**	1164.11	**1163.48**
91	31.80	90.00	250.00	1000.00	100.00	70.80	1315.00	34.47	1327.24	**1321.75**	1219.42	**1211.28**
92	25.00	30.00	250.00	1000.00	100.00	70.80	1315.00	45.11	1331.07	**1367.91**	1425.18	**1448.16**
93	25.00	0.00	250.00	1000.00	100.00	70.80	1315.00	40.60	1335.45	**1331.87**	1426.20	**1424.89**
94	31.80	65.00	250.00	2000.00	100.00	70.80	1315.00	32.18	1348.52	**1362.61**	1240.57	**1266.96**
95	31.80	120.00	250.00	2000.00	100.00	70.80	1315.00	77.97	1381.09	**1384.40**	1565.15	**1566.40**
96	31.80	120.00	250.00	2000.00	200.00	70.80	1315.00	77.97	1382.16	**1382.39**	1562.41	**1561.77**
97	31.80	65.00	250.00	1000.00	100.00	70.80	1315.00	32.18	1386.17	**1362.97**	1269.99	**1242.16**
98	31.80	90.00	250.00	3000.00	50.00	70.80	1315.00	34.47	1396.26	**1391.91**	1484.92	**1485.56**
99	31.80	40.00	250.00	2000.00	200.00	70.80	1315.00	30.79	1403.49	**1406.02**	1252.63	**1253.75**
100	31.80	40.00	250.00	1000.00	100.00	70.80	1315.00	30.79	1408.00	**1454.92**	1295.00	**1354.15**
101	31.80	90.00	250.00	1000.00	100.00	70.80	1315.00	34.47	1411.00	**1321.75**	1304.00	**1211.28**
102	31.80	0.00	250.00	2000.00	200.00	70.80	1315.00	30.00	1430.91	**1427.80**	1230.83	**1231.28**
103	31.80	65.00	250.00	3000.00	50.00	70.80	1315.00	32.18	1431.19	**1430.22**	1583.27	**1582.50**
104	31.80	40.00	250.00	2000.00	100.00	70.80	1315.00	30.79	1458.49	**1455.46**	1389.58	**1385.13**
105	31.80	0.00	250.00	2000.00	100.00	70.80	1315.00	30.00	1476.97	**1490.18**	1411.96	**1416.46**
106	31.80	40.00	250.00	1000.00	100.00	70.80	1315.00	30.79	1491.62	**1454.92**	1408.81	**1354.15**
107	36.80	90.00	250.00	1000.00	100.00	70.80	1315.00	34.47	1499.01	**1492.03**	1355.34	**1355.94**
108	31.80	90.00	250.00	2000.00	200.00	70.80	1315.00	68.94	1499.36	**1497.22**	1617.56	**1616.87**
109	31.80	90.00	250.00	2000.00	100.00	70.80	1315.00	68.94	1508.08	**1510.21**	1700.55	**1700.05**
110	31.80	0.00	250.00	1000.00	100.00	70.80	1315.00	30.00	1515.66	**1505.30**	1426.19	**1423.74**
111	31.80	40.00	250.00	3000.00	50.00	70.80	1315.00	30.79	1534.03	**1541.33**	1731.73	**1733.93**
112	31.80	65.00	250.00	2000.00	200.00	70.80	1315.00	64.35	1558.93	**1557.35**	1639.86	**1641.09**
113	31.80	65.00	250.00	1000.00	100.00	70.80	1315.00	32.18	1559.00	**1362.97**	1458.00	**1242.16**
114	21.20	0.00	305.00	3000.00	80.00	81.50	1328.00	31.31	1562.77	**1561.38**	1891.11	**1890.13**
115	31.80	65.00	250.00	2000.00	100.00	70.80	1315.00	64.35	1566.69	**1569.13**	1745.07	**1744.07**
116	36.80	90.00	250.00	1000.00	100.00	70.80	1315.00	34.47	1570.00	**1492.03**	1424.00	**1355.94**
117	31.80	0.00	250.00	3000.00	50.00	70.80	1315.00	30.00	1572.35	**1563.37**	1787.77	**1784.92**
118	31.80	0.00	250.00	1000.00	100.00	70.80	1315.00	30.00	1588.00	**1505.30**	1368.00	**1423.74**
119	31.80	40.00	250.00	2000.00	200.00	70.80	1315.00	61.58	1596.50	**1623.73**	1726.17	**1726.69**
120	31.80	0.00	250.00	2000.00	200.00	70.80	1315.00	60.00	1627.13	**1634.17**	1713.15	**1711.77**

TABLE A1 (Continued)

S. no.	X1 f_o (MPa)	X2 D_o (mm)	X3 D (mm)	X4 H (mm)	X5 S' (mm)	X6 A_b (mm^2)	X7 f_h (MPa)	X8 $\rho_v \times f_v$ (MPa)	Y1 $P_{n,1}$ (kN)	Predicted Y1	Y2 $P_{n,2}$ (kN)	Predicted Y2
121	31.80	40.00	250.00	2000.00	100.00	70.80	1315.00	61.58	1665.73	**1675.22**	1886.07	**1877.15**
122	21.20	0.00	305.00	3000.00	50.00	81.50	1328.00	31.31	1668.66	**1671.12**	2008.15	**2009.26**
123	31.80	0.00	250.00	2000.00	100.00	70.80	1315.00	60.00	1713.98	**1698.61**	1908.63	**1908.76**
124	44.00	90.00	250.00	1000.00	100.00	70.80	1315.00	34.47	1747.59	**1753.18**	1479.48	**1480.72**
125	44.00	90.00	250.00	1000.00	100.00	70.80	1315.00	34.47	1880.00	**1753.18**	1644.00	**1480.72**
126	35.00	90.00	305.00	1500.00	100.00	70.80	1562.00	39.98	2836.94	**2836.75**	2591.96	**2591.44**
127	35.00	90.00	305.00	1500.00	80.00	70.80	1562.00	39.98	2903.61	**2904.35**	2739.38	**2737.76**
128	35.00	0.00	305.00	1500.00	100.00	70.80	1562.00	36.50	2968.30	**2969.01**	2756.99	**2756.73**
129	35.00	60.00	305.00	1500.00	100.00	70.80	1562.00	37.97	2969.00	**2959.76**	2748.62	**2746.77**
130	35.00	30.00	305.00	1500.00	100.00	70.80	1562.00	36.86	3049.41	**3015.43**	2838.60	**2815.71**
131	35.00	60.00	305.00	1500.00	80.00	70.80	1562.00	37.97	3058.60	**3067.51**	2928.08	**2932.22**
132	35.00	0.00	305.00	1500.00	80.00	70.80	1562.00	36.50	3087.85	**3099.52**	2989.56	**2992.54**
133	35.00	30.00	305.00	1500.00	80.00	70.80	1562.00	36.86	3150.74	**3144.59**	3050.29	**3048.43**
134	35.00	90.00	305.00	1500.00	50.00	70.80	1562.00	39.98	3194.96	**3198.79**	3412.98	**3414.96**
135	35.00	60.00	305.00	1500.00	50.00	70.80	1562.00	37.97	3368.50	**3365.56**	3723.27	**3721.65**
136	35.00	0.00	305.00	1500.00	50.00	70.80	1562.00	36.50	3419.71	**3411.80**	3805.45	**3804.28**
137	35.00	30.00	305.00	1500.00	50.00	70.80	1562.00	36.86	3470.91	**3438.26**	3937.56	**3838.28**
138	70.20	80.00	305.00	1500.00	80.00	81.50	1328.00	33.62	4213.47	**4214.78**	3466.20	**3466.63**
139	70.20	80.00	305.00	1500.00	80.00	81.50	1328.00	50.43	4406.67	**4402.65**	3849.55	**3848.74**
140	70.20	0.00	305.00	1500.00	80.00	81.50	1328.00	31.31	4476.30	**4590.08**	3677.32	**3829.33**
141	70.20	0.00	305.00	3000.00	50.00	81.50	1328.00	31.31	4646.51	**4647.75**	4222.37	**4222.54**
142	70.20	0.00	305.00	1500.00	80.00	81.50	1328.00	46.96	4655.34	**4687.51**	4023.42	**3978.78**
143	70.20	0.00	305.00	1500.00	80.00	81.50	1328.00	31.31	4709.00	**4590.08**	3981.89	**3829.33**
144	70.20	0.00	305.00	1500.00	80.00	81.50	1328.00	46.96	4716.00	**4687.51**	3933.59	**3978.78**

Note: The bold values in the Table [A1] are the predicted results.